CalWave Power Technologies

CWPT Open Water Demonstration

DE-EE0008097.0002

Budget Period 1

Component and Subsystems Test and Verification Report

PTO Bench Testing

PTO Belt Testing

CONTENTS

Figures 4
Tables 5
Conventions 6
Abbreviations 6
1. Introduction 7
1.1 General 7
1.2 PTO Bench Testing 7
1.3 Belt Testing 7
2. PTO Test Objectives 8
2.1 Individual Component Characterization and Testing 8
2.1.1 Hydraulic Actuation 8
2.1.2 Gas spring 8
2.1.3 Electric Machine 9
2.2 Full PTO Assembly and Functionality Testing 9
2.3 Hardware-in-The-Loop Testing 9
3. PTO Testing Facilities and General Framework 10
3.1 Davis Hall Structural Testing 10
3.2 General Test Bench and Hydraulic Actuation Side 11
4. PTO Bench Description 16
4.1 PTO General Overview 16
4.2 PTO Bench overview 17
5. PTO Individual Component Characterization and Testing 19
5.1 Gas Spring 19
5.1.1 Design of Experiments 21
5.1.2 System Operating States 22
5.1.3 Testing and Procedures 22
5.1.4 Baseline Functionality Results 23
5.1.5 Sinusoidal Oscillation Results 24
5.1.6 Noise Oscillation Results 25
5.1.7 Gas-Spring System Identification 28
5.2 Electric Machine 32

5.2.1 Torque Tracking Capabilities and Torque Constant Verification 32
5.2.2 Position Control 35
5.2.3 Motor and Gearbox Couple - Friction and Stiction 35
5.3 Entire Driveshaft 37
6. PTO Belt Testing 40
6.1 PTO Belt Design Basis 40
6.2 PTO Belt Testing 41
6.2.1 CBOS Testing at IFREMER 41
6.2.2 Shock Load Testing at Exeter 41
Appendix A – Example Gas Spring SID Results 42

FIGURES

Figure 1: Global Coordinate System Position and Orientation used throughout this report. 6
Figure 2: CEE Structures Laboratory at UC Berkeley. 10
Figure 3: Speedgoat real-time controller 11
Figure 4: CAD rendering of test frame, actuator, and linear bearing system provided by Civil Engineering. 12
Figure 5: Drawing of the symmetric hydraulic actuator provided by civil engineering. 13
Figure 6: Schematic of the instrumentation and control of the hydraulic actuation side. 14
Figure 7: Time resolved data showing the hydraulic actuator displacement as measured from the string-pot and the commanded setpoint. Excellent tracking was achieved via multiple tuning iterations. 14
Figure 8: Actuation side displacement FFT of an example noise signal showing matching measured and commanded position signals across the frequency band of interest (0.1 Hz - 0.6 Hz) 15
Figure 9: Actuation side displacement FFT of an example noise signal showing only a very small phase error between commanded and measured velocity in the frequency band of interest (0.1 Hz - 0.6 Hz) .. 15
Figure 10: Rendering of PTO. Components from left to right include motor, gearbox, mooring drum, clutch, pillow block bearings, brake, spring drum, and hydraulic cylinder gas spring. 16
Figure 11: I-Beam design used as a PTO frame 17
Figure 12: CAD of PTO test stand. 18
Figure 13: CalWave's PTO drivetrain assembled onto the I-Bream frame and connected via the PTO belt to the actuation side. 18
Figure 14: CalWave's PTO drivetrain assembled on the PTO bench. Here, actuation side as well as Gas-Spring side are connected to the drive shaft via PTO belts. 19
Figure 15: Simple CAD model of the gas spring characterization and test setup. During this stage, only the Gas spring is assessed on the PTO bench. 20
Figure 16: Gas spring test stand at the Civil Engineering department at UC Berkeley. The actuation side (right silver cylinder) tracks a controlled trajectory exciting the gas spring (left black cylinder) for characterization and assessment objectives. 20
Figure 17: Schematic signal and control diagram for the Gas spring bench testing. 21
Figure 18: Measured gas spring performance under 180 second period, +/- 35 cm quasi-static sine wave excitation. Hydraulic system pressure vs hydraulic cylinder displacement (left) and hydraulic cylinder force vs displacement (right). 24
Figure 19: Measured gas spring performance under 1.5 second period, +/- 10 cm sine wave excitation. Hydraulic system pressure vs hydraulic cylinder displacement (left) and hydraulic cylinder force vs displacement (right). 24
Figure 20: Gas spring efficiency dependence on excitation period. 25
Figure 21: Hydraulic cylinder displacement (Commanded setpoint and measurement), measured hydraulic system pressure, and measured hydraulic cylinder force time resolved data for white noise excitation peak amplitude of 25 cm and frequency range of 0.1-0.6 Hz 26
Figure 22: Measured gas spring performance under 0.1 - 0.4 Hz frequency range and 29 cm (operational) and 22 cm (survival) maximum amplitude pink noise excitation. Hydraulic system pressure vs hydraulic cylinder displacement (left) and hydraulic cylinder force vs displacement under Operational (top right) and 3PTO Survival (bottom right) device states. 27

Figure 23: Comparison of various SID models derived for different poles and zero estimates. Despite small differences, all models match very well the actual signal. 29
Figure 24: System Identification results using LS method for five different models. 31
Figure 25: Torque tracking of a sinusoidal setpoint. 32
Figure 26: Torque tracking capabilities of the electric machine following a torque setpoint derived from a white noise frequency spectrum. 33
Figure 27: FFT of Motor Torque commanded signal and actual measured torque. The magnitude comparison shows excellent tracking capabilities. 33
Figure 28: FFT of torque phase tracking error in the frequency band of interest. Only a very low phase lag can be identified. 34
Figure 29: Experimental validation of the motor's torque constant. 34
Figure 30: Position tracking control of the electric motor. 35
Figure 31: Motor Torque over Motor velocity showing hysteresis, stiction, as well as velocity dependent friction. 36
Figure 32: Details of the stiction characteristics of the combined motor-gearbox couple. Only a very small torque of roughly 4 Nm is required to overcome the combined stiction. 36
Figure 33: Characteristic stiction/friction plot for the entire PTO shaft. A Least Squares grey box model with hyperbolic tangents characteristic is used to model the stiction. (15 Nm peak) 37
Figure 34: Characteristic stiction/friction plot for the entire PTO shaft. A Least Squares grey box model with hyperbolic tangents characteristic is used to model the stiction. (25 Nm peak) 37
Figure 35: Characteristic stiction/friction plot for the entire PTO shaft. A Least Squares grey box model with hyperbolic tangens characteristic is used to model the stiction. (35Nm peak) 38
Figure 36: Characteristic stiction/friction plot for the entire PTO shaft. A Least Squares grey box model with hyperbolic tangents characteristic is used to model the stiction. (40 Nm peak) 38
Figure 37: TTS Innova synthetic flat belt sample. 40

TABLES

Table 1: Summary of Instrumentation Nodes 11
Table 2: Civil Engineering Test Stand Capabilities 12
Table 3: Friction and Stiction Model Parameter for the entire PTO drive shaft. 39

CONVENTIONS

CalWave is using the following convention for the positioning and orientation of the global coordinate system. This convention is equal to the most common convention used in Naval Architecture and specifically in wave energy conversion related research & development:

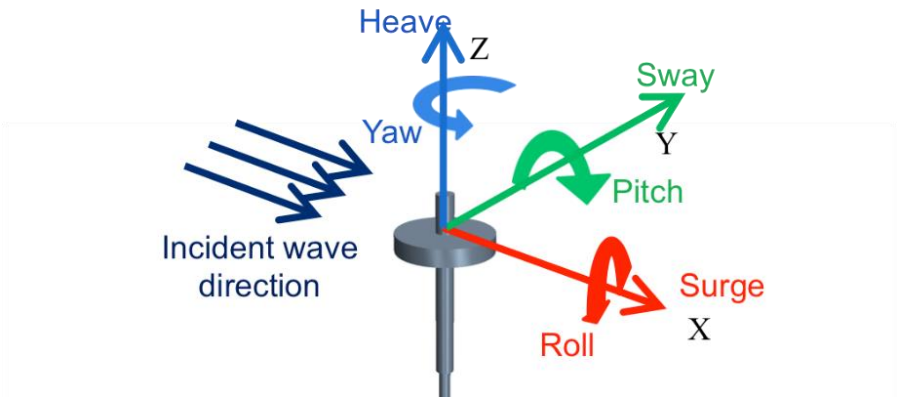

Figure 1: Global Coordinate System Position and Orientation used throughout this report.

ABBREVIATIONS

PTO	Power Take-Off
PTO	Power Conversion Chain
WEC	Wave Energy Converter
HIL	Hardware in the Loop

1. INTRODUCTION

1.1 GENERAL

The objective of the project is to advance the Technology Readiness Level (TRL) of the Wave Energy Converter (WEC) developed by CalWave Wave Power Technologies Inc (CalWave) through advanced numerical simulations, dynamic hardware tests, and ultimately a scaled open water demonstration deployment while continuing to exceed DOE's target ACE threshold of 3m/M$. The outcomes of Budget Period 1 will be a detailed design of the scaled demonstration unit and bench testing of the critical hardware components. In Budget Period 2, the key outcomes will be deployment and operation of the demonstration unit at an open water site which replicates full scale ocean conditions, and performance and load measurements will be used to validate the high techno-economic performance (ACE) of the device full scale device, as measured by the "Average Climate Capture Width per Characteristic Capital Cost" (ACE) metric defined for the Wave Energy Prize.

1.2 PTO BENCH TESTING

Project Task 3.1 seeks to de-risk the actuated hardware components which will comprise the demonstration WEC's Power Take-Off (PTO). A single 1:5 scale PTO was assembled, characterized, and tested for various performance metrics in a controlled laboratory environment. After characterizing component parameters for use in accompanying numerical simulations of the WEC, the full PTO was tested using a hardware-in-the-loop (HIL) scheme to evaluate performance in waves representative of the deployment site.

1.3 BELT TESTING

The PTO primarily acts in a rotary frame, but ultimately the WEC reacts against the sea floor via a linear mooring line. The linear-rotary conversion is accomplished with a simple belt-and-drum concept. In fact, this conversion occurs twice in each PTO, once at main mooring line interconnection, and once at the drive shaft's interface with the hydraulic cylinder gas spring.

In project Task 3.2, the belts used for converting linear to rotary motion for both the mooring and the hydraulic gas spring were tested by two additional partners with specialized experience in testing synthetic tension members, each focusing on a known potential failure mode. The belt design basis and testing campaigns are discussed in **section 6**.

2. PTO TEST OBJECTIVES

CalWave experimentally tested a **1:5 scale prototype PTO** at the University of California, Berkeley's Davis Hall. These tests include the following objectives:

2.1 INDIVIDUAL COMPONENT CHARACTERIZATION AND TESTING

To ensure a fully characterized PTO system as well as functionality of all sub-components of the PTO, the main actuated and/or controlled components were characterized individually on the bench:

2.1.1 Hydraulic Actuation

- Assess and quantify accuracy of position tracking capabilities: Input displacement signal derived from either pre-defined time series or from fixed time step time domain simulations needs to be tracked accurately to ensure validity of PTO bench testing. This is an important step to ensure the output of the simulation/actuation leads to representative input into the simulation via the physical PTO on the bench.
- Assess and quantify lead/lag dynamic characteristics for the entire frequency spectrum under various load conditions and under representative load conditions. Potentially compensate using feed forward controller.
- Assess dead band/stiction for actuation signals and potentially compensate using feed forward controller.
- Assess and quantify actuator bandwidth & dynamic response spectrum under representative load conditions.
- Ensure all emergency stops and interlocks work as designed.

2.1.2 Gas spring

- Verification that measured gas spring force, displacement, system pressures and other characterizing measurements are within the range of initial design parameters.
- Verification that components acquired and chosen are suitable for all operational states of the gas spring.
- Quasi-Static characterization of the gas spring with focus on 1) Force-Displacement relation for different accumulator charge pressures, 2) Hysteresis assessment.
- Assess and quantify dynamic characteristics for the entire frequency spectrum of interest under various load conditions and varying accumulator charge pressures.
- Assess frequency and load dependent dead-band/stiction/friction.
- Dynamic model System Identification to estimate force from gas spring displacement and/or accumulator pressure to 1) use in numeric models and 2) use as an input into PTO control schemes. The model will either be derived as a single input – single output model or as a multi input – single output model.
- Ensure all emergency stops and interlocks work as designed.

2.1.3 Electric Machine

- Power Electronics Commissioning
  - Configuration of assembled power electronics components
  - AC supply identification
  - DC link voltage control
- Stiction/Friction Characterization
- Torque Constant (K_T) validation
- Hardware enable signals configuration
- Safety stop triggers definitions

2.2 Full PTO Assembly and Functionality Testing

- Assemble full PTO and perform run out measurements and shim accordingly to ensure shaft alignment within assembly spec tolerances
- Confirm actuation capability of clutch and brake
- Actuate system with oscillatory motion or random disturbance. Impose desired force tracking curve and confirm motor capability to enforce curve
- Check force estimation capabilities using measured parameters and compare with realized force on the load cell. Confirm that PTO can be operated without loadcell as a sensor input

2.3 Hardware-in-The-Loop Testing

- Simulate all design operational wave states (e.g. IWS, CWS) and assess dynamic PTO behavior
- Evaluate PTO performance metrics with focus on total device performance and PTO induced losses as well as PTO
- Ensure motor can track torque setpoints sufficiently well
- Ensure PTO controller used in the simulation works as expected taken typical device oscillations and PTO characteristics into account

3. PTO TESTING FACILITIES AND GENERAL FRAMEWORK

3.1 DAVIS HALL STRUCTURAL TESTING

The Pacific Earthquake Engineering Research Center (PEER) operates the Structures Laboratory within UC Berkeley's Civil and Environmental Engineering, which houses equipment for studying the behavior of structural elements and systems both on scale models and larger prototypes. Studies range from detailed stress analyses to both static and dynamic tests on full-sized structural systems.
At the CEE Structures Laboratory, conventional tests can be conducted using the lab's uniquely large strong floor, flexibly configured reaction systems, and variety of actuators and modern instrumentation devices and sensors. The facility is capable of inducing forces ranging from few pounds to millions of pounds. It can apply and measure deformations ranging from a few thousandth of an inch to tens of inches.
Testing capabilities include:

- Modern techniques for hybrid simulation methods that combine physical and analytical sub-structures into a hybrid model of the entire structure using state-of-the-art digital controllers,
- The Open-source Framework for Experimental Setup and Control (Open-Fresco)
- The latest finite element models built using the Open System for Earthquake Engineering Simulation (Open-Sees) framework

The laboratory includes a base-isolated 41 ft. x 131 ft. concrete strong floor, to which the reaction frames, actuators, and specimens are securely fastened during the tests. The 10-ton bridge crane can accommodate test specimens up to 17 ft. in height. The Structures laboratory is shown in Figure 2.

Figure 2: CEE Structures Laboratory at UC Berkeley.

3.2 General Test Bench and Hydraulic Actuation Side

3.2.1 Instrumentation and Bench Controller

The test bench instrumentation is built around the EtherCAT protocol, a real-time industrial communications standard development by Beckhoff. EtherCAT provides deterministic exchange of data among distributed input/output nodes via modules ("terminals") for a broad array of data types. The test bench uses EtherCAT to connect the central controller, motor controls, and the various sensor and actuator IO points along the PTO. The figure below summarizes the important nodes along the EtherCAT network.

Table 1: Summary of Instrumentation Nodes.

Node	Product (Provider)	Function
Central Controller	Speedgoat (Mathworks)	Aggregate sensor data and supply control commands to all other nodes
Motor Controller	S120 (Siemens)	Precise control of electric motor and management of electric power input/out
Distributed IO	E-series IO terminals (Beckhoff)	Modular IO points for sensing and controlling PTO components • Analog sensor inputs • 24V hydraulic valve actuation

For accurate control and ultimately to be used for the hardware-in-the-loop simulation a Speedgoat controller is used. As directly supported by Mathworks, Speedgoat offers a real time target machine that can directly execute Simulink control as well as Simscape Toolboxes code. This allows not only for rapid prototyping of control loops and but moreover, to use existing WEC Simulink models (e.g. WECSim) for external execution on the real time controller.

A baseline Speedgoat target machine with the following parameter were used:

- Baseline real-time target machine - S
- Intel 2GHz quad core CPU
- 4GB RAM
- 32GB SSD for data logging
- four mPCIe I/O slots for I/O expansion
- 1 x Intel GbE for host-target communication and XCP Slave (Vector CANape and ETAS INCA
- Calibration and Monitoring support)
- 1 x USB for kernel transfer, PS/2 and USB connectors to attach a keyboard
- 1 x Display Port for target screen. 2 x GbE for EtherCAT Master (R2016a+) and/or real-time UDP (R2016b+) and/or XCP Master

Figure 3: Speedgoat real-time controller

3.2.2 Hydraulic Actuator

The hydraulic actuator includes a symmetric hydraulic cylinder trunnion mounted to a steel frame. The frame consists of two large welded I-beams and a large precision machined aluminum plate. The linear

bearing system is comprised of four linear bearings mounted to a small aluminum plate that ride on a pair of rails mounted to the large aluminum plate. This linear bearing system in turn supports the hydraulic cylinder rod end through a clevis bracket and allows for connection to test specimens. A summary of the hydraulic actuator capabilities can be found in Table 2. Thus, there will be a slight limitation in the realizable speeds of the test stand. A rendering of the test stand is shown in Figure 4 with drawing details of the hydraulic actuator in Figure 5.

Table 2: Civil Engineering Test Stand Capabilities.

Parameter	Value	Units
Force	89	kN
Displacement	+/- 0.91	m
Max Velocity	~1	m/s

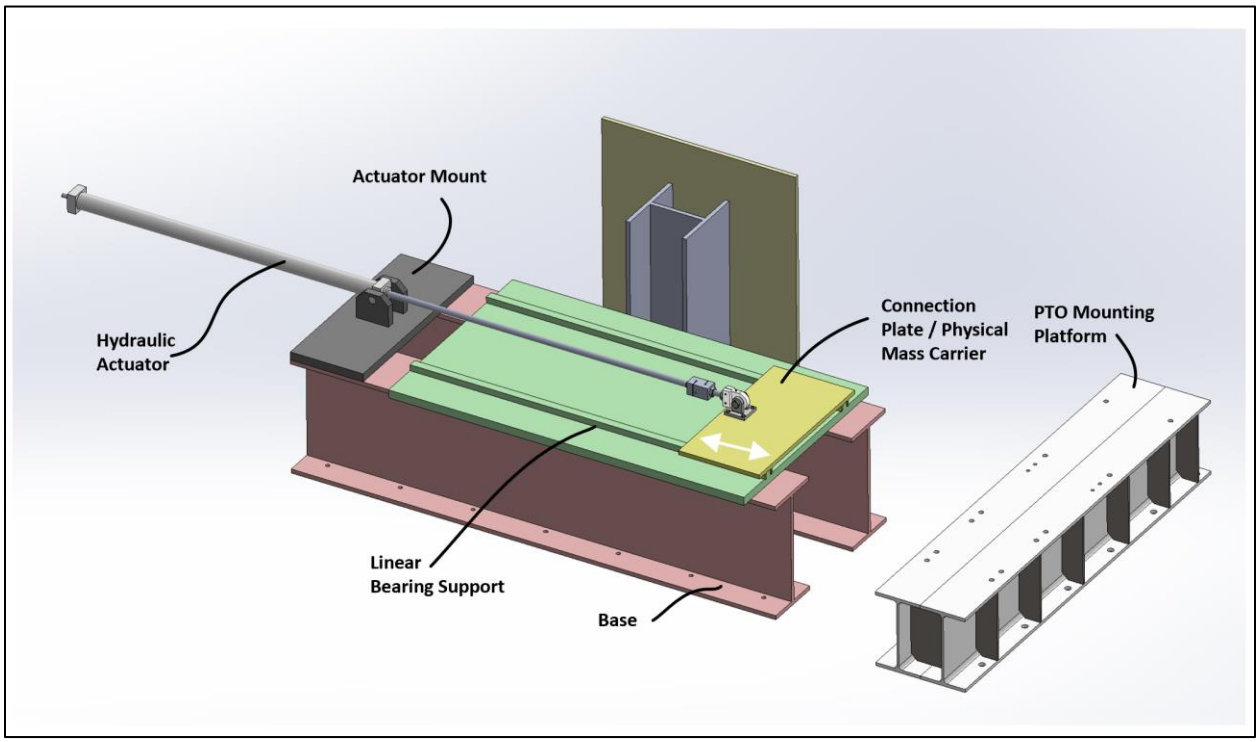

Figure 4: CAD rendering of test frame, actuator, and linear bearing system provided by Civil Engineering.

The hydraulic cylinder is driven through a NC Servo Technology valve from building hydraulic supply at 207 bar (3000 psi). The building hydraulic supply can apply flow rates up to 1082 lpm (286 gpm), much greater than peak flow rates required by the hydraulic actuator. The servo valve is powered and controlled through an MTS 407 controller that is configured to receive external analog excitation commands from the Beckhoff systems.

The controller also serves as a signal conditioner for the actuation side sensors and includes a PID as well as a feed forward compensation term. Additionally, interlocks can be set which stop the actuation in case the displacement or force signals show values out of the defined bounds for inherent safety during testing conditions.

An analog displacement command is fed into the hydraulic valve controller. However, next to the feed forward compensator in the hydraulic valve controller an additional feed forward compensator is used to adjust the actuation command signal before sending it to the hydraulic valve controller. Very precise setpoint displacement tracking in the desired frequency range was achieved.

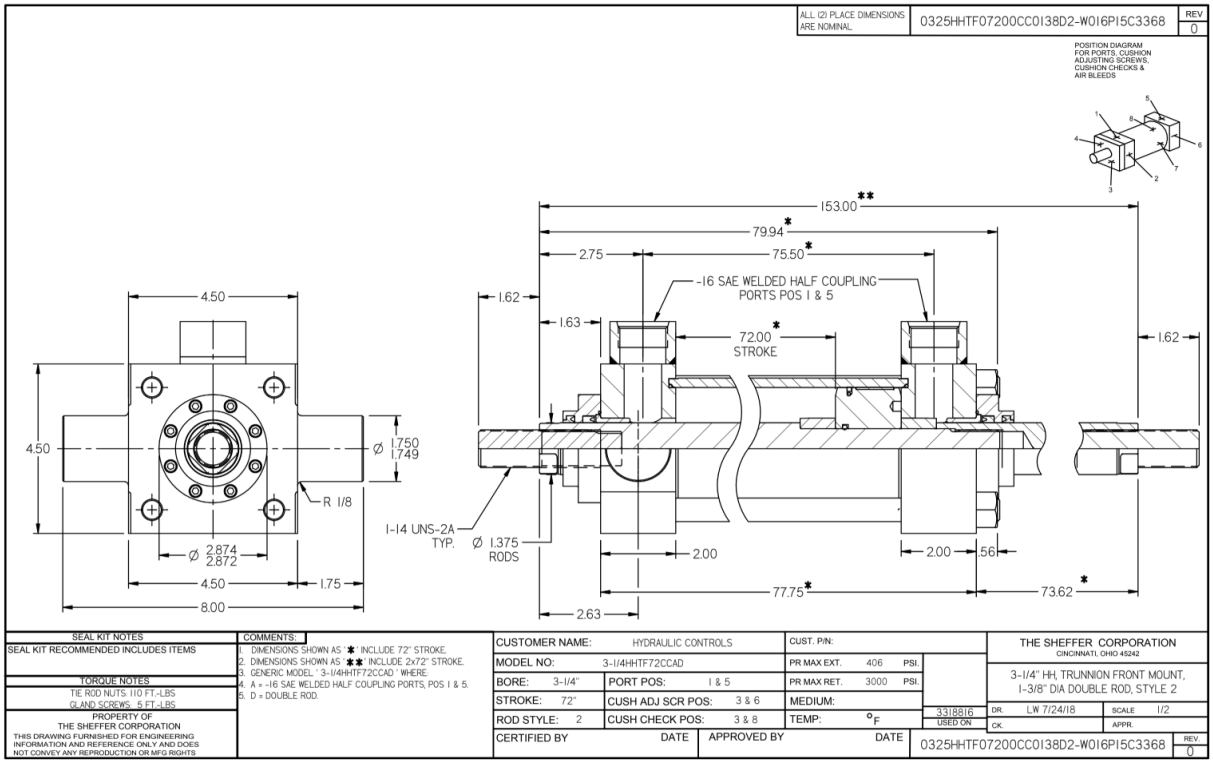

Figure 5: Drawing of the symmetric hydraulic actuator provided by civil engineering.

3.2.3 Actuation Control and Tracking Capabilities

To ensure accurate tracking capabilities of the actuation side the hydraulic actuation side was position controlled. For accurate tracking, feed forward compensators in the real time controller (SpeedGoat), as well as PID & Feed Forward parameter in the hydraulic valve controller (MTS Controller) were tuned using sine and noise setpoint signals in a representative bandwidth.

To ensure correct tuning, a representative load equivalent to common loads acting on the devices mooring belt was induced via the Gas Spring. As the actuation side will be used as the representative PTO belt load input, this ensures that the hardware-in-the-loop experiments will be executed with a well-tuned actuation side to minimize loop errors. Figure 6 shows an overview of the actuation side including all sensors and controllers involved.

The actuation side tuning process involved multiple iterations on controller gain tuning and subsequent execution of a setpoint signal with multisines and post-processing to ensure both, magnitude as well as phase is matching between the measured position signal and the position setpoint sent by the real-time controller (SpeedGoat).

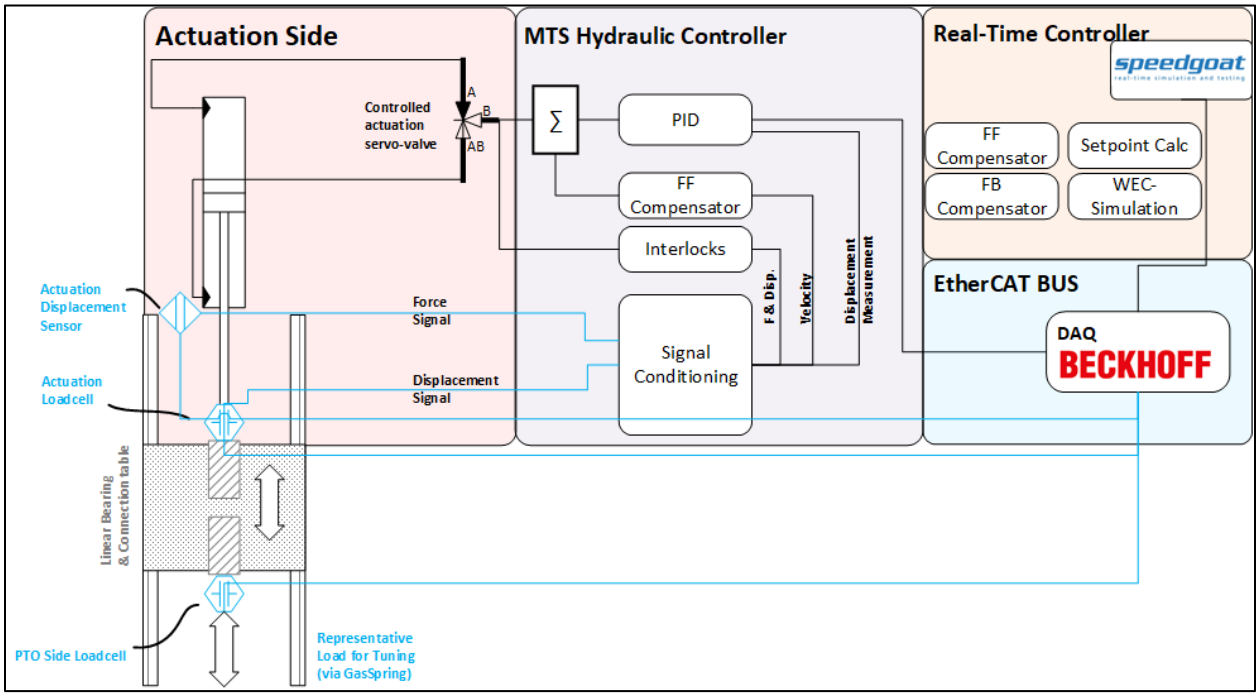

Figure 6: Schematic of the instrumentation and control of the hydraulic actuation side.

Figure 7 shows an example of a white noise signal time snippet including the measured displacement signal from the actuation side string-pot as well as the overlapping commanded positioning signal. Excellent tracking was achieved via multiple iterations of tuning.

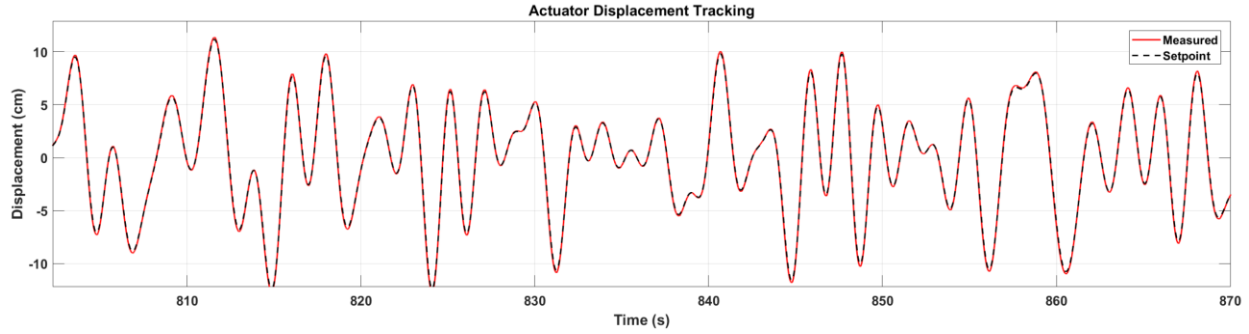

Figure 7: Time resolved data showing the hydraulic actuator displacement as measured from the string-pot and the commanded setpoint. Excellent tracking was achieved via multiple tuning iterations.

To obtain a more holistic view of the tracking capabilities of the hydraulic actuation side, white noise multisine signals were used as a displacement setpoint. Following parameter were used for the noise signal:

- ➔ Frequency band of interest: 0.1 Hz – 0.6 Hz
- ➔ Displacement amplitude of 5cm, 10cm, 15cm, 20cm, 30cm, 40cm
- ➔ Repeat Time of 500s with N=3 repeats

The noise signals provide a good overview of the tracking capabilities in terms of a) magnitude and b) phase between the commanded and the recorded position signal. Figure 8 shows the FFT of an example noise signal with a displacement of 15 cm amplitude. It can be seen that the magnitudes across the entire frequency band are matching indicating a well-tuned actuation side. Additionally, Figure 9 shows for the same case the frequency resolved phase error: Across the entire frequency band only a very small error of maximal 0.02 radians, respectively 1.1 Degree occurs, further showing the good tracking capabilities of the actuation side.

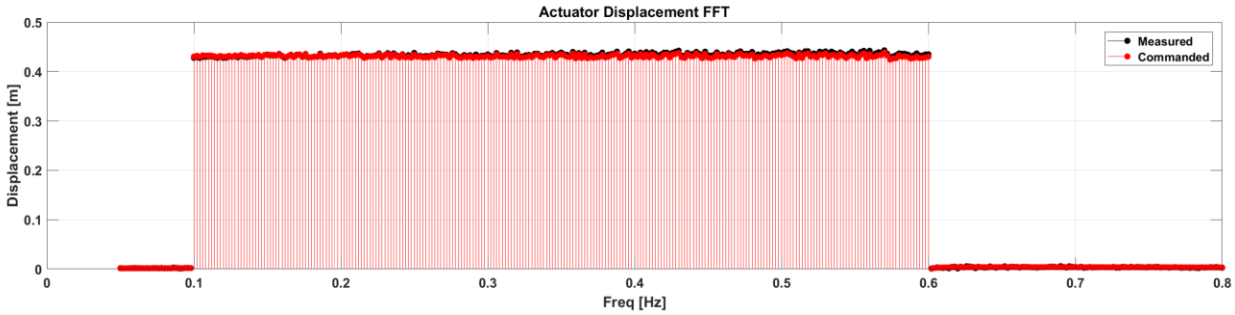

Figure 8: Actuation side displacement FFT of an example noise signal showing matching measured and commanded position signals across the frequency band of interest (0.1 Hz - 0.6 Hz).

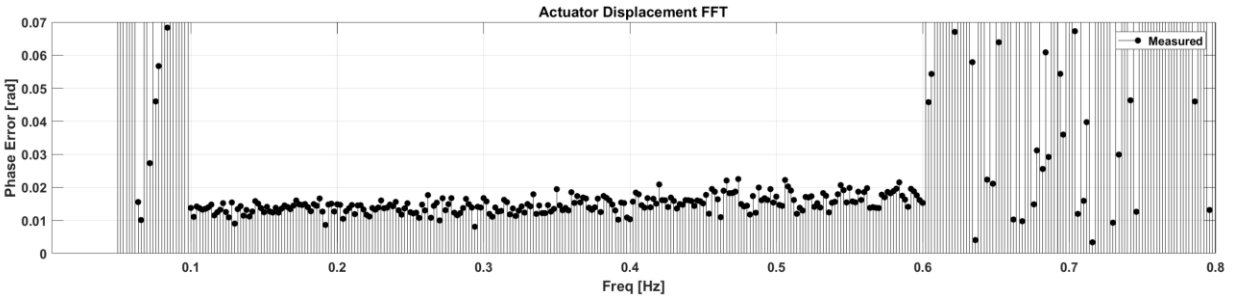

Figure 9: Actuation side displacement FFT of an example noise signal showing only a very small phase error between commanded and measured velocity in the frequency band of interest (0.1 Hz - 0.6 Hz).

4. PTO Bench Description

4.1 PTO General Overview

The WEC will include a total of four PTOs, each rigidly attached to the device and sealed within the WEC's water-tight pressure hull. The PTO is shown below in Figure 10. Each PTO uses a single winch and motor for both energy capture and depth changing operations. The mooring line anchors directly to the sea floor. A belt connects the mooring line to the mooring winch drum (**1**) which allows for linear to rotary motion transfer.

The generator/motor (**2**) is connected to the mooring winch drum through a speed reducing gearbox (**3**) and can exert "four quadrant" torque on the winch drum (power into and out of the device in either rotational direction). A gas spring consisting of a hydraulic cylinder (**4**) and accumulator provides a passive restoring force to the system and is always in tension. Because the device is positively buoyant, the gas spring maintains the necessary pretention for the device to oscillate around an equilibrium position instead of passing that force offset onto the motor/generator. This gas spring is converted from the linear to rotary frame through a second belt and drum (**5**).

A clutch (**6**) between the mooring winch drum and the gas spring drum allows the two drums to spin independently when needed (e.g. during depth change operations, when the WEC must translate to a new oscillation midpoint along the mooring belt). A brake (**7**) allows the gas spring drum to be held in place. The mooring winch drum/belt is exposed to the environment but seals (**8**) on the rotary shaft keep all other components dry in an enclosed chamber.

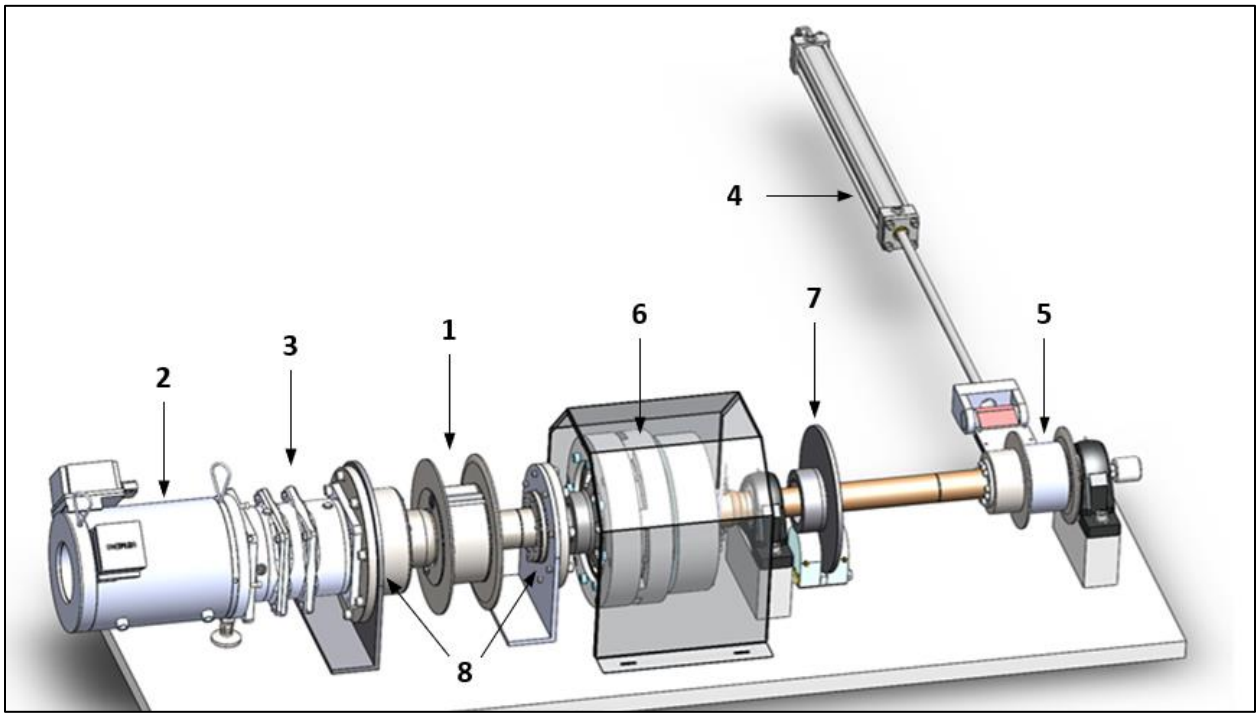

Figure 10: Rendering of PTO. Components from left to right include motor, gearbox, mooring drum, clutch, pillow block bearings, brake, spring drum, and hydraulic cylinder gas spring.

During normal operations, the PTO oscillates around an equilibrium position defined by the gas spring. To change depths, the brake is engaged when the PTO velocity is at or near zero, holding the gas spring in place, and the clutch is disengaged. The full mooring line tension is then applied to the motor, which adjusts the length of the mooring belt. Once the desired displacement has been achieved, the clutch is engaged, and the brake is released, allowing the PTO to oscillate around a new equilibrium position.

4.2 PTO BENCH OVERVIEW

To assess PTO system dynamics, performance, and for verification of the general behavior of the designed PTO, a single unit of the PTO design was assembled at the PTO test bench. All components required, including instrumentation and control hardware, mounting brackets and hardware, as well as a rigid frame to mount the PTO on, was assembled on the strong floor of UC Berkeley's Civil Engineering laboratory.

UC Berkeley engineering staff assisted in the assembly process. Figure 11 shows a drawing of the I-Beam used as a frame to rigidly mount the PTO drivetrain onto.

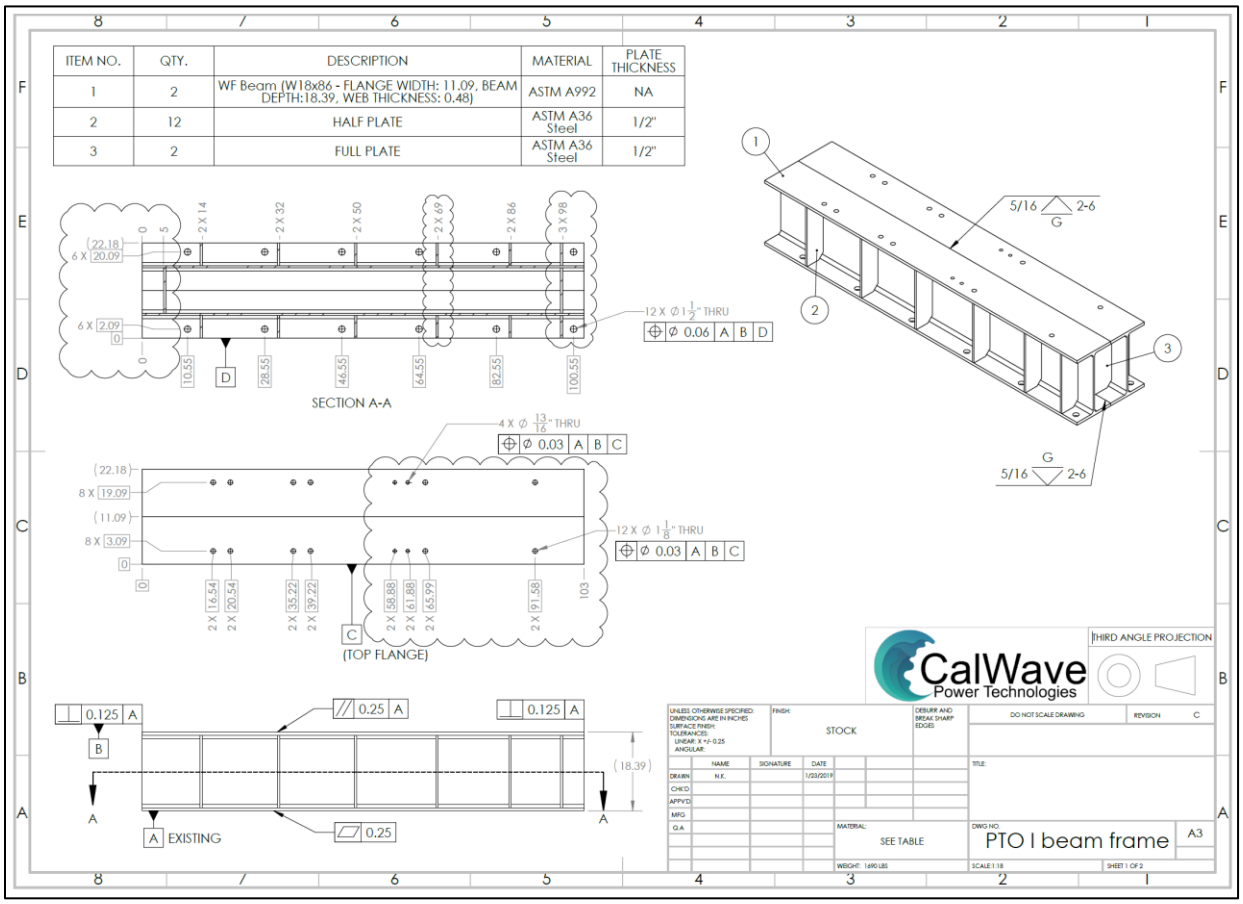

Figure 11: I-Beam design used as a PTO frame.

CAD of the full PTO bench set up is shown in Figure 12 while Figure 13 shows a picture of the realized PTO bench setup. All drivetrain components were mounted to the PTO I-Beam frame and the PTO is connected

via the belt to the actuation side. Note, that depending on the component characterization objective belts were connected or disconnected from either the actuation side or the gas-spring.

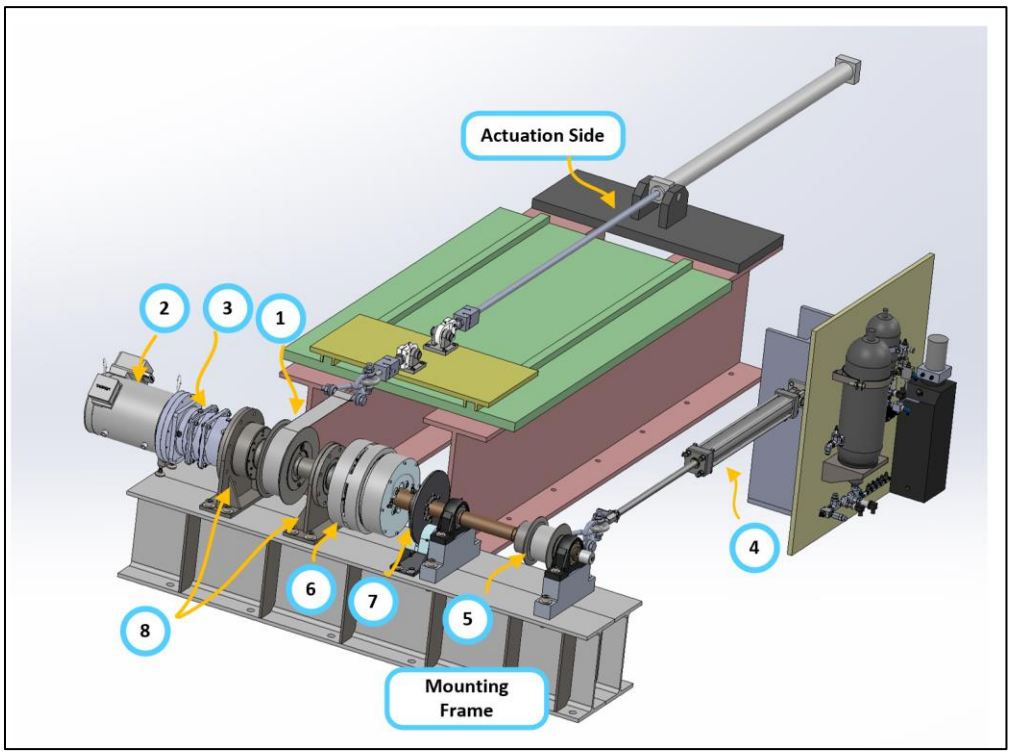

Figure 12: CAD of PTO test stand.

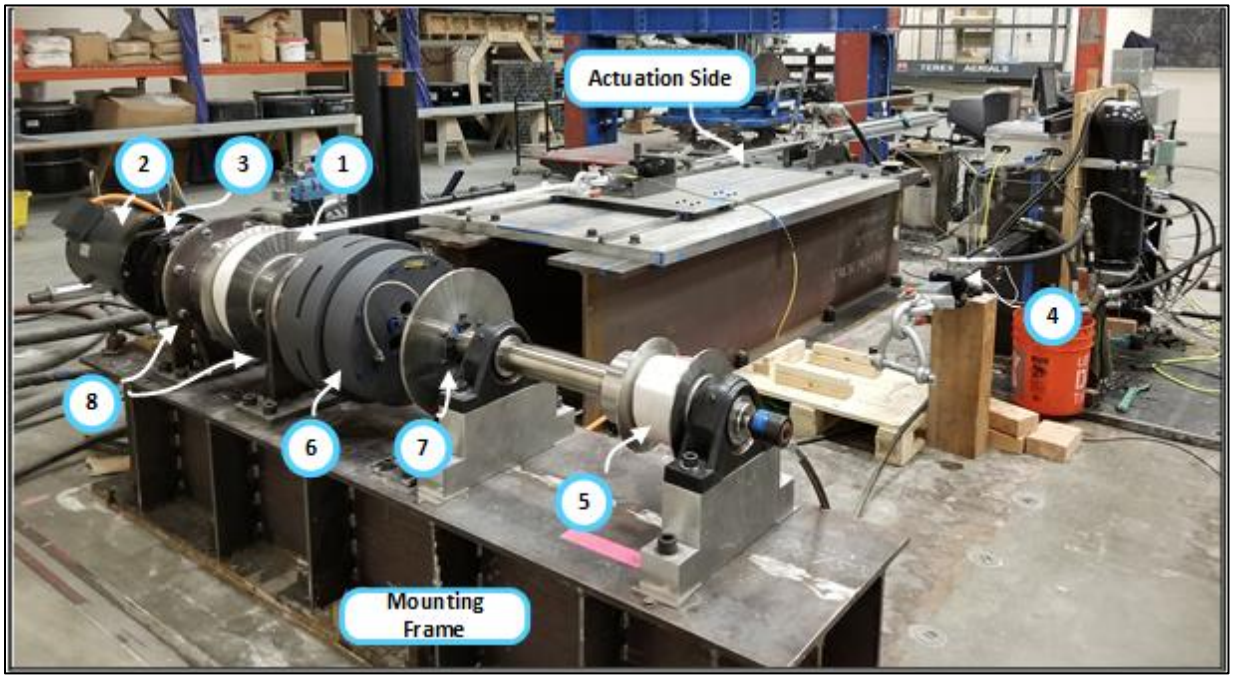

Figure 13: CalWave's PTO drivetrain assembled onto the I-Bream frame and connected via the PTO belt to the actuation side.

Figure 14 shows another view of the PTO bench assembly. Here, actuation side as well as Gas-Spring side are connected to the drive shaft via PTO belts. In the front, the Gas-Spring accumulator and the cylinder can be seen.

Figure 14: CalWave's PTO drivetrain assembled on the PTO bench. Here, actuation side as well as Gas-Spring side are connected to the drive shaft via PTO belts.

5. PTO Individual Component Characterization and Testing

Prior to full PTO assembly, individual subsystems were assembled and tested/characterized individually to reduce risk and complexity.

5.1 Gas Spring

The gas spring was characterized and tested separate from the rest of the PTO drive line. For comprehensive testing the gas spring was assembled and mounted to the civil engineering frame was done as shown in Figure 15, including a loadcell at the end of the hydraulic cylinder and a string potentiometer displacement sensor. These sensors, in addition to a pressure sensor, temperature sensor, and solenoid valve control were connected to the DAQ and control system. Note that the gas spring configuration pictured was for a previous design iteration that included 3x 3.8 L accumulators as opposed to the single 18.5 L accumulator used in the full PTO assembly; the change was made to simplify the number of components and achieve a less stiff spring that was closer to the initial design target. The assembled gas spring test stand is shown in Figure 16.

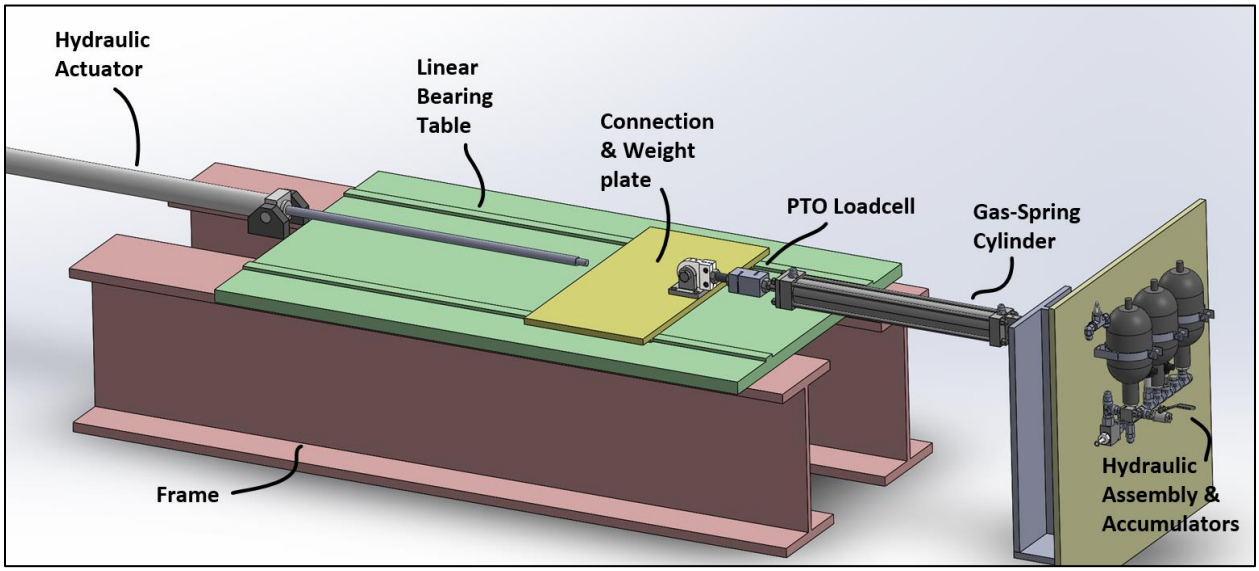

Figure 15: Simple CAD model of the gas spring characterization and test setup. During this stage, only the Gas spring is assessed on the PTO bench.

In this configuration, the cap side of the cylinder and relief valve was connected directly to a temporary reservoir. Barring any unexpected behavior, the oil that enters the reservoir drained only at the seal leak rate of the hydraulic cylinder piston seals which is, compared to the system's full oil volume a neglectable amount. This configuration was later revised such that both were ported directly to the HPU drain.

Figure 16: Gas spring test stand at the Civil Engineering department at UC Berkeley. The actuation side (right silver cylinder) tracks a controlled trajectory exciting the gas spring (left black cylinder) for characterization and assessment objectives.

Figure 17 shows a schematic of the gas spring test bench including all sensor and control commands.

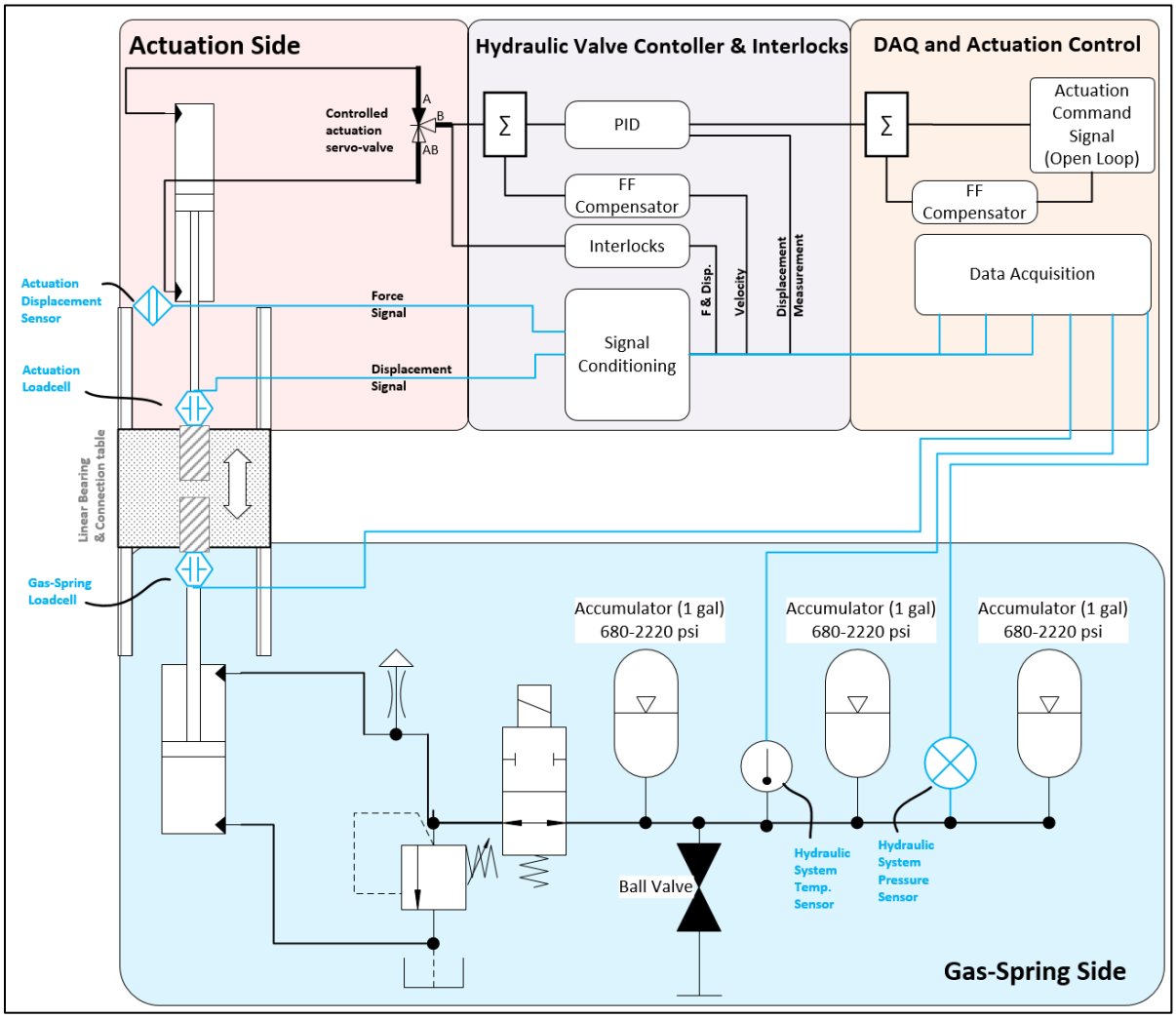

Figure 17: Schematic signal and control diagram for the Gas spring bench testing.

5.1.1 Design of Experiments

Multiple characterization experiments to assess the behavior of the gas spring and to characterize the system are summarized in the following:

1. Baseline functionality tests including quasi-static displacement of the spring piston using the actuation side. Observation of system pressure, forces, vibrations and commanded vs. actual displacements to ensure the system is working as expected.

2. Sinusoidal oscillations with different strokes and periods around the equilibrium spring displacement position. These experiments help to identify any nonlinearities in a controlled manner for the range of expected frequencies. Additionally, the experimental results can be used in a least square fit to derive parameter estimations for a gas spring grey-box model.

3. Noise excitation with different amplitudes in the expected range of frequencies in the system. Both white and pink noise spectrums are utilized. Additionally, to identify any nonlinearities in

excitation multiple actuation gains are included in the assessment which scale the effective excitation amplitude. Experiments are repeated with multiple different phase realizations of the same spectrum for suitability of multi-input – multi-output (MIMO) system identification and model derivation.

5.1.2 System Operating States

The different device "operational" states are covered by four different hydraulic accumulator fluid charge states. For each of these states the gas spring was tested to assess performance over the range of these expected system modes. Even though the gas spring system charge allows for continuous states in between, the following discrete states were tested on the bench:

1. **Normal operation:** The system is operating in a power producing submergence depth, absorbing energy at usual force and displacement levels. This status is the most occurring state and will be used for nearly all regular operational cases.

2. **Operation with only 3 PTOs (1 offline):** This state is an abnormal state which is not expected to occur during regular operations. However, in case of a single PTO failure the static offset buoyancy of the device is split over 3 rather than 4 PTO units. Thus, the hydraulic system pressure will increase. These tests help to verify and build confidence that the hydraulic spring can effectively still operate in case of a PTO failure.

3. **Operation in survival mode:** This state will assess the hydraulic spring behavior in the case of survival submergence of the device for sheltering and load reduction. Due to the increased submergence depth the hydraulic system pressure rises.

4. **Operation in survival mode with only 3 PTOs**: This ultimate failure state claims to be the largest load testing case to be assessed at the bench. The state emulates the failure of a single PTO unit in addition to a deep submergence of the device leading to the largest hydraulic system pressure to be assessed.

5.1.3 Testing and Procedures

In the following different test procedures are introduced.

Initial circuit charging procedure:

While the circuit is still void of hydraulic fluid, follow manufacturer's recommended charging procedure to bring accumulators to desired nitrogen pre-charge pressure. Be sure to allow 15 min after initial charging to allow transient thermal effects to settle and verify pre-charge pressure. Once desired pre-charge pressures have been met, confirm cylinder is at minimum stroke and turn on HPU. Ensure instrumentation is properly connected and that readings are valid, especially for pressure. Energize directional valve to fill hydraulic circuit with fluid, until fluid pressure matches accumulator pre-charge. Deenergize directional valve and excite cylinder a few cycles. Once at rest, crack open the bleed valve to allow any accumulated gas to escape. Repeat process until bleed valve only discharges oil.

Pre-charge adjustment

When a pre-charge pressure change is desired, ensure cylinder is at its minimum stroke position. Energize the directional valve to allow all fluid to drain from the accumulator and fluid pressure drops to 0 psig. Adjust accumulator gas charge to desired pressure and reenergize the directional valve to pump hydraulic fluid back into the system to the desired pressure. Air bleeding should not be necessary. Deenergize the directional valve and turn off HPU.

Relief valve setpoint setting

Begin the with cylinder at minimum stroke and accumulator hydraulically charged to a large pretension state. Tighten relief valve adjustment screw about halfway of its travel to set at 1500 psi initially. Using the loadcell to estimate pressure, slowly extend the cylinder until the relief valve activates. Note the released force and adjust screw accordingly to target 150 bar. Once satisfied, tighten lock nut on relief valve to hold set point and return cylinder to minimum position. If significant fluid was relieved, additional hydraulic fluid may need to be added to the circuit.

Measurements and Triggering

Sensor data for gas spring force, displacement, hydraulic system pressure, and temperature is recorded at 100 Hz. All experiments were controlled on the same Speedgoat and Beckhoff Controller/DAQ system which was also used for data collection. Thus, experiment control signals were inherently synchronized to measured sensor signals and no external triggering was required.

5.1.4 Baseline Functionality Results

Baseline functionality of the test stand and the gas spring was first conducted via quasi-static displacement of the gas spring. Results of an example experiment are shown in Figure 18 for sinusoidal excitation with 35 cm amplitude and 180 second period. Two full periods are shown, indicating repeatability of the procedure. The period tested is roughly 40 times longer than typical wave excitation periods at this scale and was thus determined to be quasi-static. Significant hysteresis can be seen in both the pressure vs displacement as well as the force vs displacement as different curves are traced out as the accumulator gas is expanding or contracting, indicating the gas temperature dependence of the process. The discontinuity at the displacement extrema in force vs displacement plot comes from the change in friction when changing displacement directions. Stiction is estimated to be about 1.1 kN from this experiment. System pressure levels and forces within target design values were achieved.

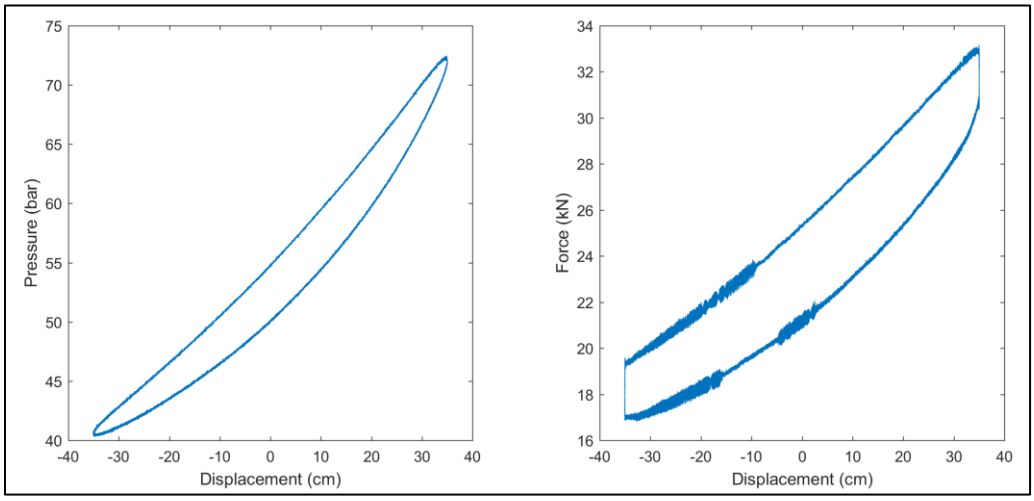

Figure 18: Measured gas spring performance under 180 second period, +/- 35 cm quasi-static sine wave excitation. Hydraulic system pressure vs hydraulic cylinder displacement (left) and hydraulic cylinder force vs displacement (right).

5.1.5 Sinusoidal Oscillation Results

Following the quasi-static excitation experiments, various sinusoidal excitations with more relevant frequencies were tested. Excitation frequencies varying between 1 and 4 seconds were tested. Results from an example experiment are shown in Figure 19 for sinusoidal excitation with 10 cm amplitude and 1.5 second period. 36 full periods are shown, again indicating the repeatability of the experiment. Note at the higher frequency, the accumulator behaves adiabatically compared to the quasi-static case, and there is thus no longer any hysteresis in the pressure vs displacement plot. However, because of viscous friction related effects, there is much more hysteresis in the force vs displacement plot.

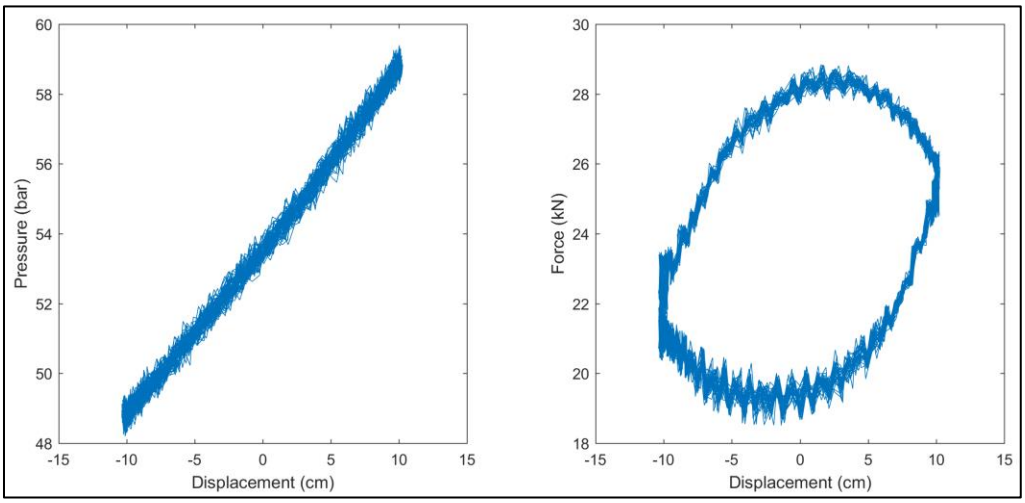

Figure 19: Measured gas spring performance under 1.5 second period, +/- 10 cm sine wave excitation. Hydraulic system pressure vs hydraulic cylinder displacement (left) and hydraulic cylinder force vs displacement (right).

Gas spring efficiency was calculated by dividing the total work done by the gas spring by the total net work done on the gas spring during a single experiment. A summary of these efficiencies is shown in

Figure 20 for 10 cm amplitude excitations. The increase in efficiency with excitation period is likely due to viscous friction in the system becoming less dominant. For most relevant wave excitation frequencies at the current scale, efficiencies of 80% and above can be expected.

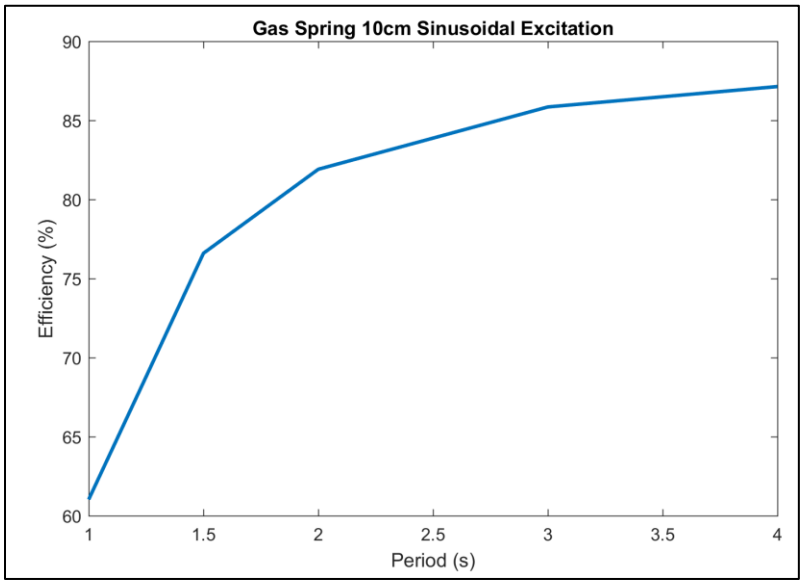

Figure 20: Gas spring efficiency dependence on excitation period.

5.1.6 Noise Oscillation Results

Following sinusoidal excitation experiments, the gas spring was excited with noise spectrums. For dynamic characterization of the gas spring a 0.1 – 0.6 Hz frequency band multi-sine signal / white and pink noise is used. The gains, labeled via maximum amplitudes of the noise signal, range between 10 cm up to 35 cm in amplitude. The desired actuation bandwidth was chosen to cover the range of expected frequency excitations of the gas spring in the demonstration device and utilize most of the total gas spring stroke (allowing a margin for safety with actuator overshoot and gas spring internal cushions).

Time history plots are shown in Figure 21 for an example white noise experiment with maximum displacement amplitude of 25 cm and frequency range of 0.1-0.6 Hz. The displacement plot shows excellent agreement between commanded and actuator realized gas spring displacements. The measured pressure is quite smooth and well correlated with the displacement. Small jumps in the force signal can be seen due to friction along with some small vibrations that were excited in the setup.

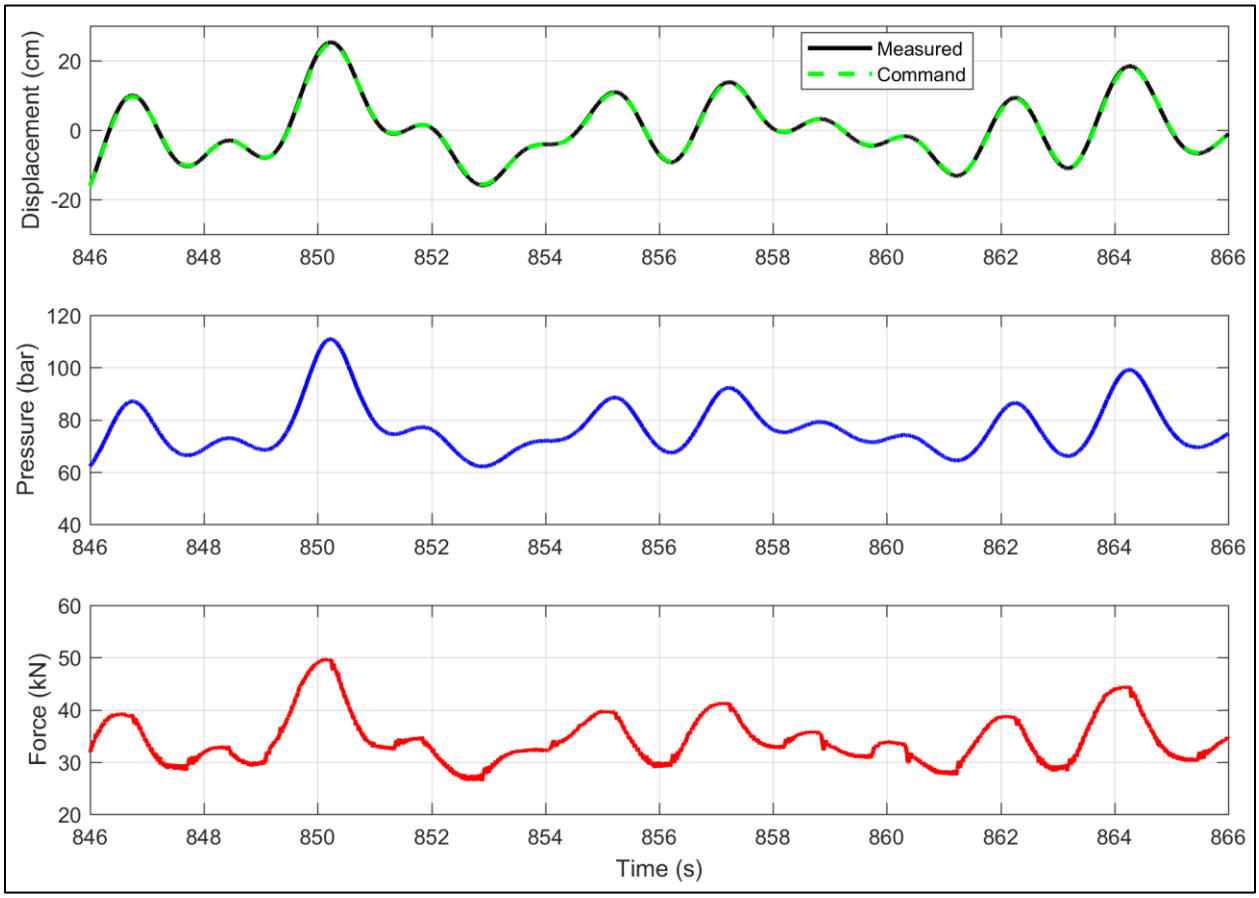

Figure 21: Hydraulic cylinder displacement (Commanded setpoint and measurement), measured hydraulic system pressure, and measured hydraulic cylinder force time resolved data for white noise excitation peak amplitude of 25 cm and frequency range of 0.1-0.6 Hz.

Results from two example experiments are shown in Figure 22 for a pink noise frequency range of 0.1-0.4 Hz. Results are shown for a gas spring set point during normal operations as well as during operations at survival depth. Maximum excitation amplitudes of 29 cm (operational) and 22 cm (survival) were used. Each data set contains over 24 minutes of experiment run time. The measured pressure vs displacement data agrees well with the initial target design in the operational case but shows some error at the higher pressure survival depth operating point although the range of achieved pressures is still within specifications. This indicates that a more sophisticated gas model than the simple polytropic one may need to be evaluated to improve pressure prediction accuracy in all system states. Unlike pressure, the measured gas spring force is affected by more than just the displacement, indicated by the hysteresis and width of the traced shapes. This is likely due to static and viscous friction effects.

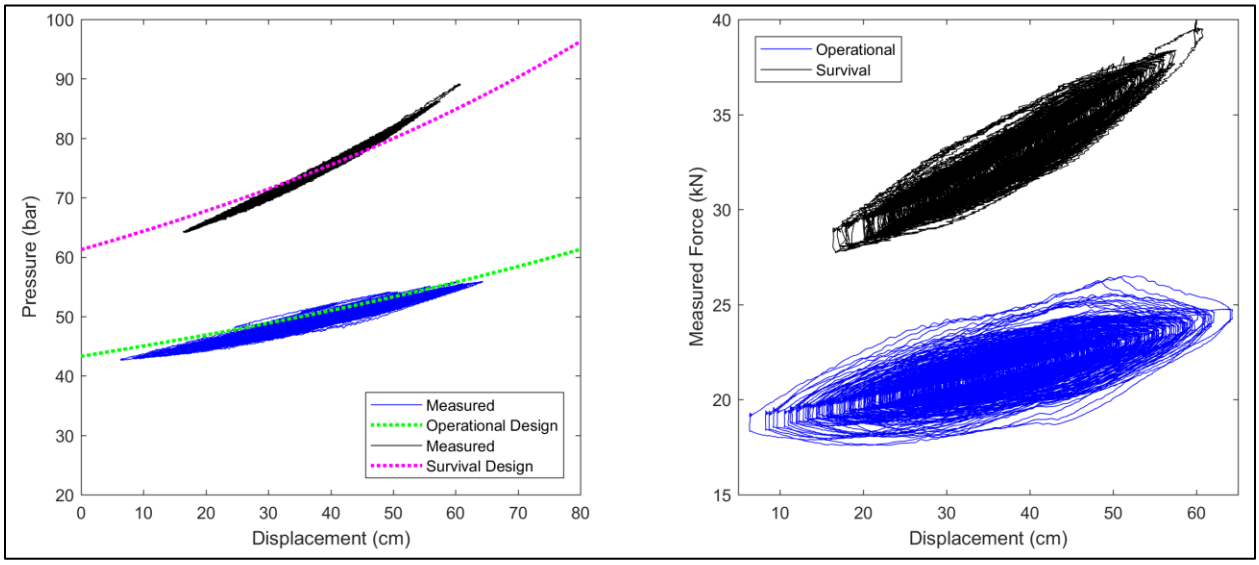

Figure 22: Measured gas spring performance under 0.1 - 0.4 Hz frequency range and 29 cm (operational) and 22 cm (survival) maximum amplitude pink noise excitation. Hydraulic system pressure vs hydraulic cylinder displacement (left) and hydraulic cylinder force vs displacement under Operational (top right) and 3PTO Survival (bottom right) device states.

5.1.7 Gas-Spring System Identification

Gas Spring System Identification was conducted in a wide range of displacements as well as for various pre-charge pressures of the accumulator. Experimental system identification follows the well-known procedures using multi-sine input noise signals. Depending on the frequency binning and the total run-time of the noise signal this method allows to obtain a large quantity of information for various frequencies in the band of interest.

For Gas-Spring system identification the following properties were used to derive appropriate time-resolved noise signals:

- ➔ Frequency band of interest: 0.1 Hz – 0.4/0.5 Hz
- ➔ Displacement amplitude of 10cm, 15cm, 20cm, 25cm, 30cm, 35cm
- ➔ Repeat Time of 500s with N=3 repeats
- ➔ Three different phase realizations for Multiple Input identification
- ➔ Various pre-charge pressures

Matlab's System Identification Toolbox was used to post process data and derive appropriately designed SID models. More specifically, transfer function estimators (tfest) as well as state space-based sub-space algorithm (ns4) system identification was conducted.

In general, it is of high interest to derive computational models that are very lean in terms of computational expenses, yet accurate to represent the physical model. Thus, a simple least-square analysis with varying input terms of different orders was additionally conducted. Results and comparison with the SID models are shown in this chapter.

Objective for the System Identification is to derive A: an accurate gas-spring model that can be used in the controller for the physical PTO in the WEC and B: an accurate gas-spring model that can be used in the mid-fidelity numerical simulation of the WEC.

Both, a blackbox model approach to derive a gas-spring model in form of a transfer function as well as a grey box model approach to derive a gas-spring parametric model was conducted. Both approaches are presented in the following sections:

A: Blackbox Model

The necessity of an accurate gas-spring model for the PTO controller is caused by the lack of gas-spring force sensor. In order to build an estimator for the total PTO force as a control parameter as well as to correctly derive the setpoint torque signal for the motor, the time resolved force that the Gas-Spring exerts onto the PTO shaft needs to be known.

A separated gas-spring model in the numerical simulation thus allows to further break down the force components contributing to the total mooring/PTO belt force. For the physical device controller all sensor information that will be available in the actual ocean-going PTO are available for system identification purposes:

- Cylinder displacement, velocity, and acceleration
- Hydraulic Accumulator/System pressure
- Accumulator temperature

Thus, the system is a multi-input signal. As the sole output of the desired model is the Gas-Spring force, the model becomes a MISO-system. Since not all the above signals necessarily have to be included in the model any combination of the above signals may be suitable for identification of an accurate model.

A comparison on what MISO system leads to the leanest yet comprehensive estimator has been conducted for the operational system states at all displacement gains. Transfer function estimates has been conducted with a variety of poles and zeros while Matlab's optimization fiction was used to determine the best tradeoff between accuracy and computational expenses for different state space orders.

For an exemplary amplitude of A = 15 cm gain the following Figure 23 shows a comparison of *actually measured* gas spring force and system identification output models for various orders:

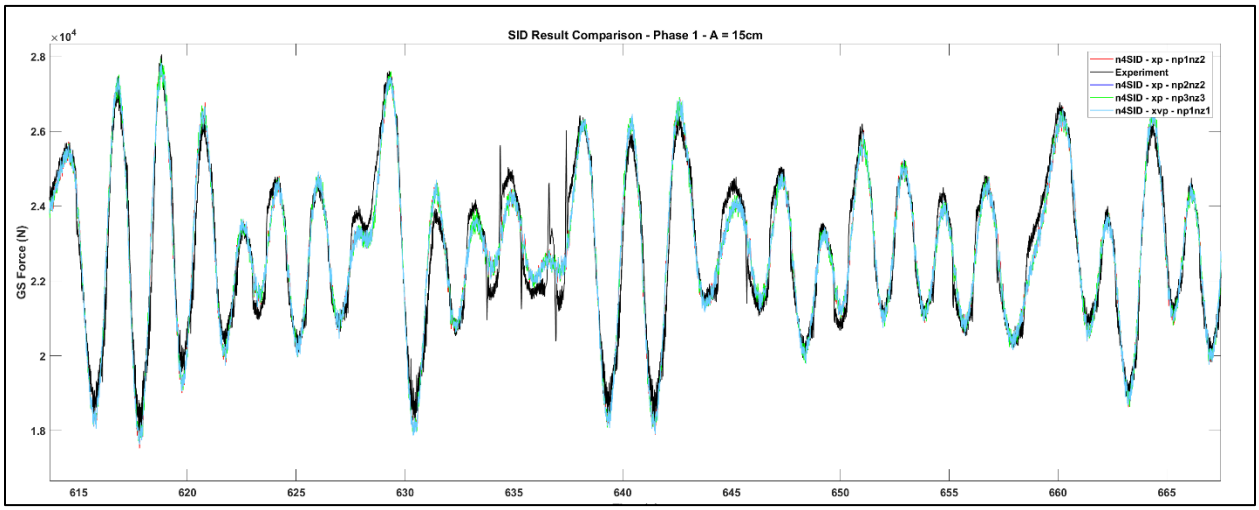

Figure 23: Comparison of various SID models derived for different poles and zero estimates. Despite small differences, all models match very well the actual signal.

The procedure was repeated for all displacement gains and identified models for large gains (e.g. 35cm) showed also a good food for lower gains (e.g. 10cm). Additional example time resolved plots for larger gains can be found in the Appendix A.

B: Grey-box Model

Next to a black-box system identification method, a grey-box parametric system identification via a least square fit with various input signals and various signal exponents was conducted. This procedure is comparable to a first order system identification and additionally allows to include physical understanding of the system (e.g. friction characteristic as a velocity dependent characteristic) into the model.

To obtain a Least Square fit, for each of the input signals vectors for each repeat of the gas-spring noise excitation experiments were created to serve as the base variables for the Least Square fit:

```
LS.F = [F_GS(:,1); F_GS(:,2); F_GS(:,3)];                    % Gas-Spring Force
LS.FIni = [F_GSIni(:,1); F_GSIni(:,2); F_GSIni(:,3)];
LS.x = [x_Meas(:,1); x_Meas(:,2); x_Meas(:,3)]/100;          % Given in cm
LS.v = [v_Act(:,1); v_Act(:,2); v_Act(:,3)];                 % Given in m/s
LS.vIni = [v_ActIni(:,1); v_ActIni(:,2); v_ActIni(:,3)];     % Given in m/s
```

```
LS.p = [p(:,1); p(:,2); p(:,3)];                                    % Pressure in bar
```

The above baseline variables were used in different combinations to shape the data vector for the least square fit. Five different models were tested as candidates for the least square approximation and model identification. The models reached from an affine, linear model (Model LS.A) up to a 10 parameter complex model (Model LS.E) which includes explicit friction and stiction terms:

- **Linear (affine) model - displacement based (3 Parameter)**

```
LS.A = [ones(N,1), LS.x, LS.v];
```

- **Linear (affine) model - pressure based (4 Parameter)**

```
LS.B = [ones(N,1), LS.p, ...                    % Pressure related
sign(LS.v), LS.v];                             % Velocity related
```

- **Complex Model; no hysteresis; no stiction (8 Parameter)**

```
LS.C = [ones(N,1), LS.x, LS.x.^2, LS.x.^3, ...     % Position related
LS.v, LS.v.^2, LS.v.^3];                           % Velocity related
gamma = 0.001;                                     % Stribeck velocity
threshold
beta = 10*sqrt(2)*gamma;      % Coulomb velocity threshold from Stribeck
```

- **Complex Model; Hysteresis term; no stiction (8 Parameter)**

```
LS.D = [LS.p, ...                                    % Pressure related
tanh(LS.v/beta), LS.v, LS.v.^3, LS.x, LS.x.^2,LS.x.^3];% Velocity related
```

- **Complex Model; Hystersis term, stiction term (10 Parameter)**

```
LS.E = [ones(N,1), LS.x, LS.x.^2, LS.x.^3, ...      % Position related
LS.v, LS.v.^2, LS.v.^3, ...                         % Velocity related
(sqrt(2*exp(1))*exp(-(LS.v/gamma).^2).*LS.v/gamma), ... % Estimates the
Breakaway Friction Force
tanh(LS.v/beta)-(sqrt(2*exp(1))*exp(-(LS.v/gamma).^2).*LS.v/gamma)];    %
Estimates the Coulomb Friction Term
```

Subsequently, for the main operating gas-spring displacements the above models were compared in their ability to model the dynamic gas-spring force. Figure 24 shows a comparison for an example 15cm displacement gas-spring noise experiments including the model fit for all of the five LS models described above.

Qualitative comparison of the different models showed that some models (e.g. Model A and C) can lack characteristics of the model. On the other hand, even simple models that are pressure based can relatively well capture the entire gas-spring characteristics (e.g. Model B). More complex models such as the 8 or 10 parameter friction and stiction model do not lead to a significantly better fit.

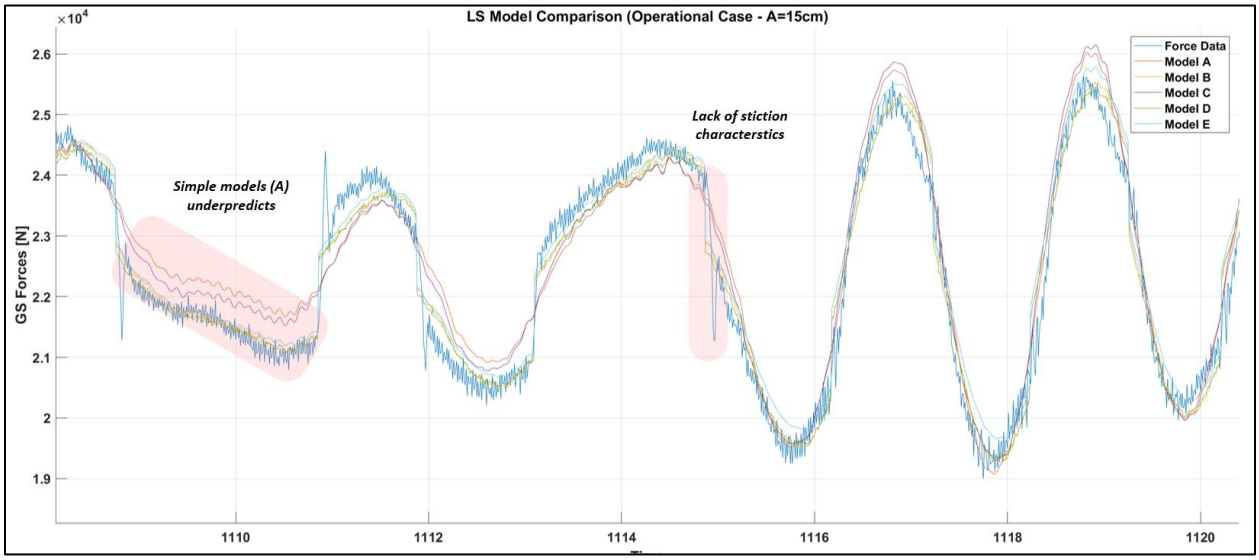

Figure 24: System Identification results using LS method for five different models.

Compared to the black box system identified models the LS method allows a faster and still accurate system identification of the gas-spring which was expected as the single hydraulic cylinder connected to an accumulator can even be analytically described very well.

5.2 ELECTRIC MACHINE

5.2.1 Torque Tracking Capabilities and Torque Constant Verification

During normal operations the motor will operate in a torque control mode to manage the tension and displacement in the linear mooring lines. A first, basic test of this functionality was conducted to verify the torque control precision and motor torque constant.

In these tests the motor is connected via the mooring drum and belt to the hydraulic actuator, which is driven linearly back-and-forth in a position-controlled pattern. The motor is commanded to maintain a constant torque setpoint throughout the motion.

For commissioning purposes sine torque setpoints were used to assess the general capability of the electric machine to track a desired torque signal. A time history of an example experiment is shown on the left of Figure 25. The right side shows a zoomed-in view of the torque setpoint and measured torque (derived from motor current measurement); the measured torque follows the setpoint satisfactorily, with some expected noise due to mechanical imperfections and measurement error.

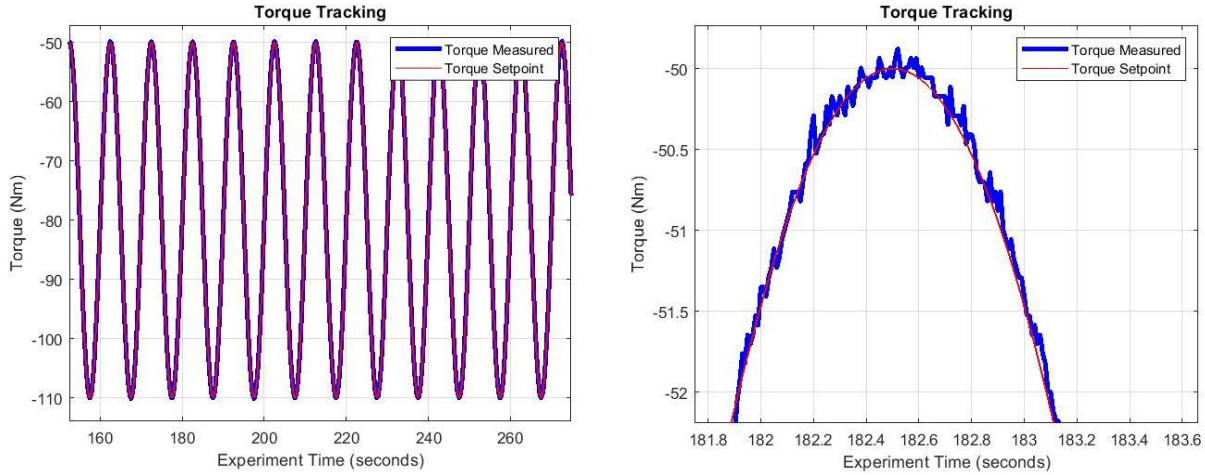

Figure 25: Torque tracking of a sinusoidal setpoint.

To assess the electric machines' capability to precisely follow a torque setpoint in a broad band of frequencies white noise signals were used with a bandwidth of 0.1 to 0.5 Hz. Figure 26 shows an example time resolved tracking plot which, again, shows the excellent capability of the motor to track a specific setpoint. Additionally, the correlating motor current is plotted.

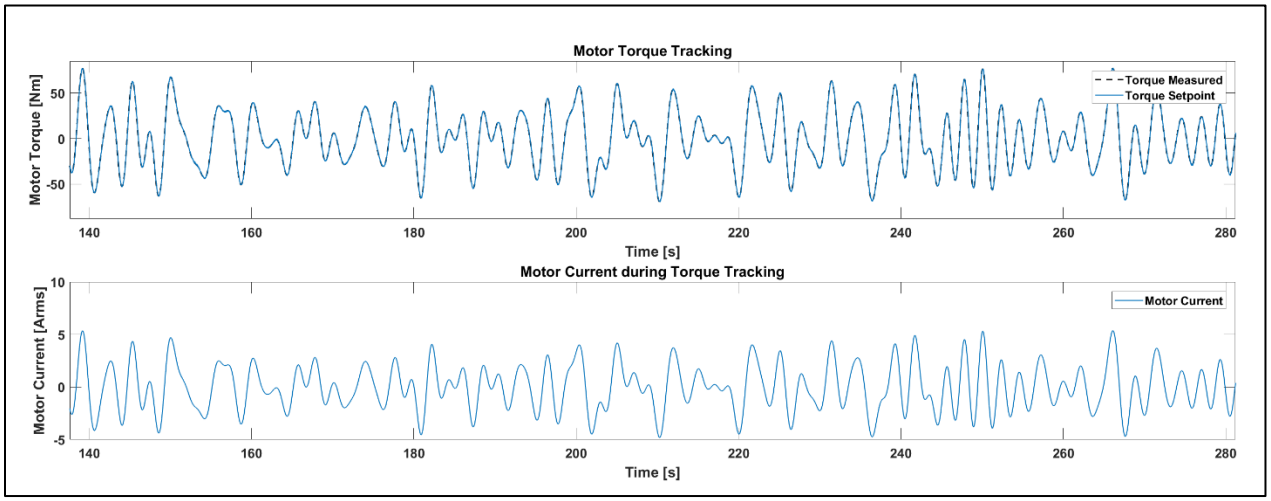

Figure 26: Torque tracking capabilities of the electric machine following a torque setpoint derived from a white noise frequency spectrum.

To gain a more quantitative assessment of the tracking capabilities Figure 27 shows the magnitude FFT of the tracking setpoint and the measured torque across the frequency band. The comparison indicates excellent tracking capabilities.

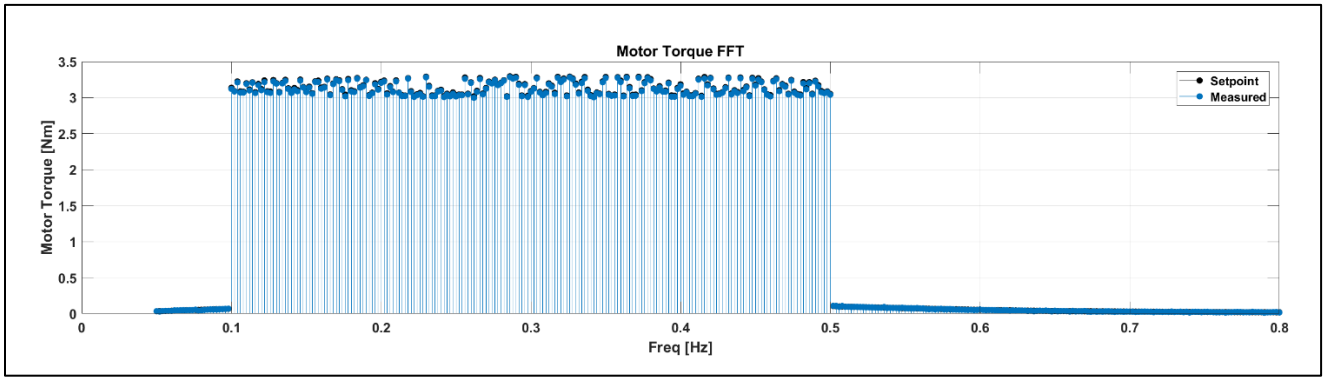

Figure 27: FFT of Motor Torque commanded signal and actual measured torque. The magnitude comparison shows excellent tracking capabilities.

Similar to the magnitude, the phase error in torque tracking can be qualitatively assessed by plotting the tracking phase delay of both signals for each frequency bin via FFT analysis. Figure 28 shows this tracking phase delay which indicates only a very low lag.

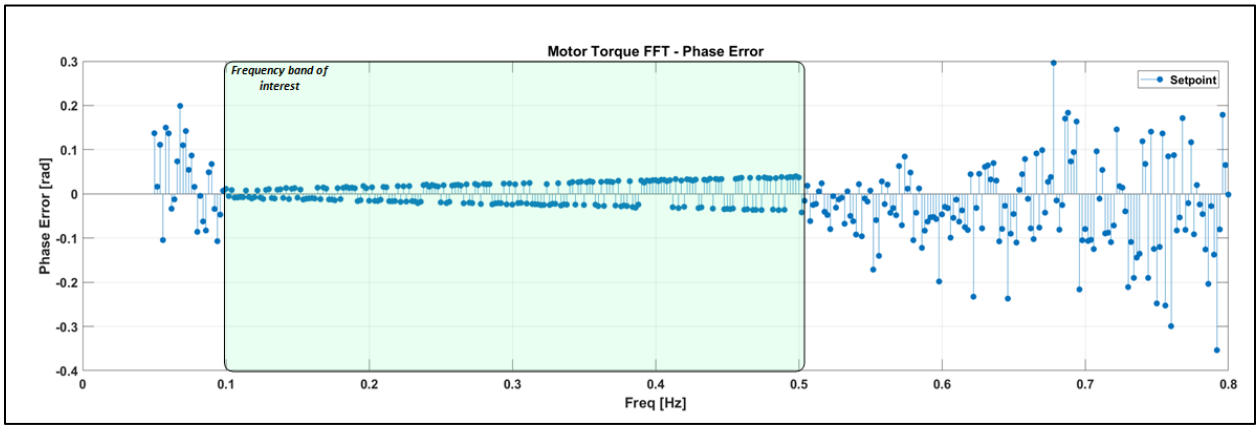

Figure 28: FFT of torque phase tracking error in the frequency band of interest. Only a very low phase lag can be identified.

The torque constant ("K_T") of a permanent magnet electric machine is defined by the exact geometry and dynamic relationship of the rotor magnets and stator coils and is an important characteristic for controls development and performance evaluation.

Though K_T can be very closely approximated in the motor design and fabrication, small differences in the assembly and dynamic changes during operation can change the value. Validation of the motor's factory-supplied torque constant of 14.4 Nm/A, using the constant torque experimental data, is show in Figure 29.

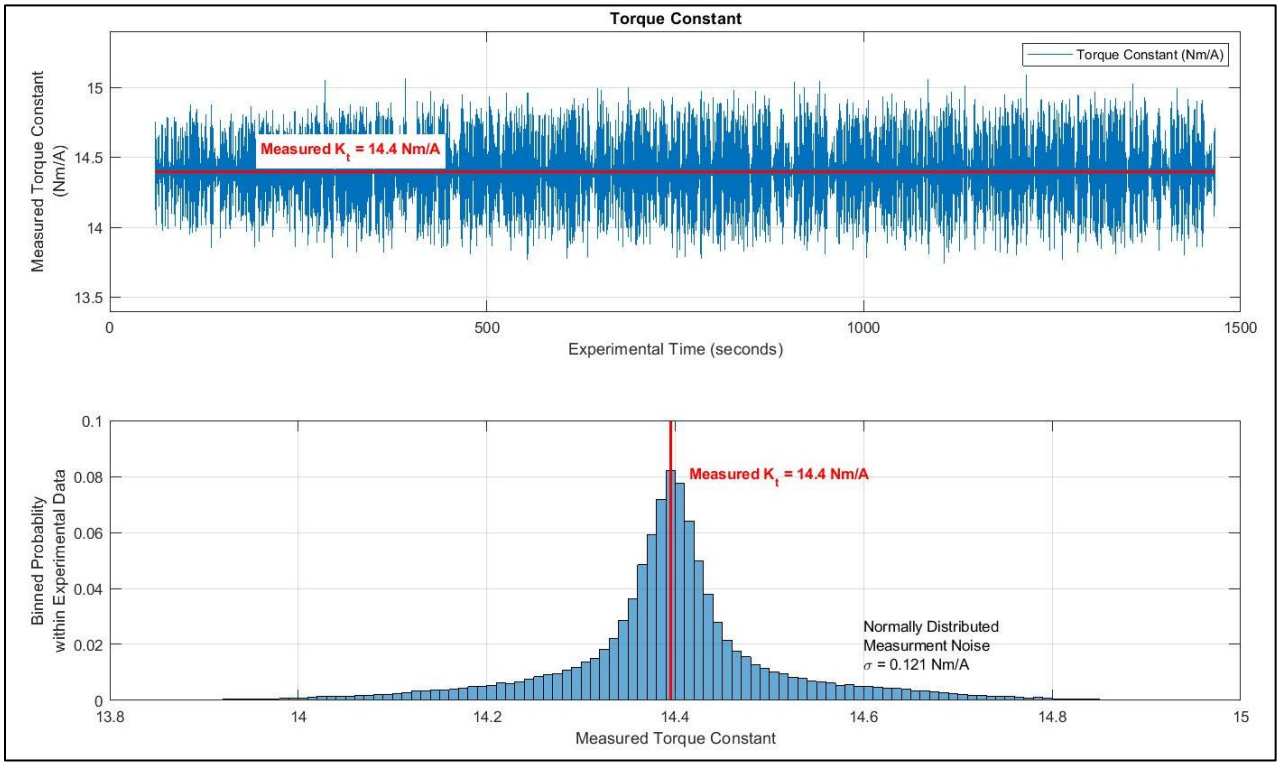

Figure 29: Experimental validation of the motor's torque constant.

5.2.2 Position Control

The motor must operate in a rotational position control mode at times during the WEC deployment, e.g. during depth change operations. On the test bench the motor is used in position control mode to affect the gas spring white noise excitation described in the Noise Oscillation Results, section 5.1.6. Position setpoints and measured position are shown in Figure 30. The position control is precise, thanks to the motor's high-resolution encoder.

A slight time delay (~10ms) persists between the position command and the achieved position; this is primarily because a simple proportional controller was used in these experiments for expedience, and a more robust PID controller with feed-forward gain will be implement for later tests to reduce the time lag.

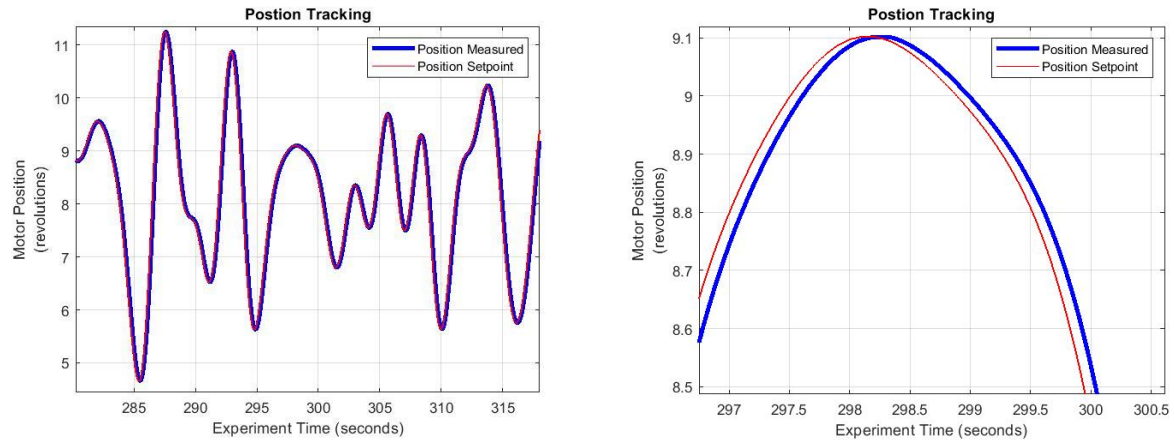

Figure 30: Position tracking control of the electric motor.

5.2.3 Motor and Gearbox Couple - Friction and Stiction

As torque from the motor is applied through the gearbox onto the shaft, friction from bearings and seals accumulate. Friction compensation in the torque control command requires accurate measurement and model of the friction characteristic, preferably of each component individually. The gearbox friction and stiction characteristics are can be extracted from the data in Figure 31: Motor Torque over Motor velocity showing hysteresis, stiction, as well as velocity dependent friction., in which a white noise torque command was applied to the motor and gearbox without any other load. The linear relationship between velocity and torque suggests a simple viscous (velocity-dependent) friction term. The vertical offset of that linear relationship defines the stiction term (the torque required to begin moving the gearbox from standstill). This stiction term (~4 Nm) can be seen more clearly in Figure 32; also visible is the hysteresis behavior of the stiction characteristic, in which small time lags in magnetization of the motor's shaft and microscope deformations of the gearbox materials create a "dead-band" where the linear stiction-friction characteristic must account for the shaft inertia. Once quantified, these phenomena are compensated for in the motor control models.

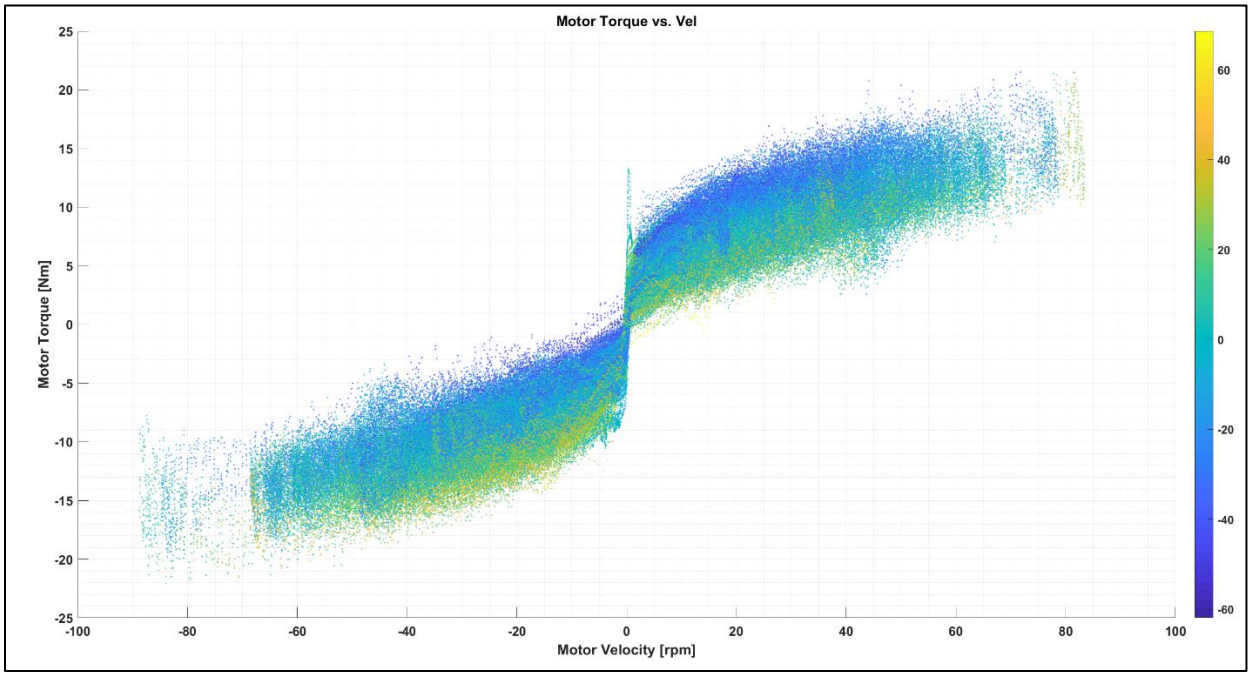

Figure 31: Motor Torque over Motor velocity showing hysteresis, stiction, as well as velocity dependent friction.

Color shows that there is absolute position dependency.

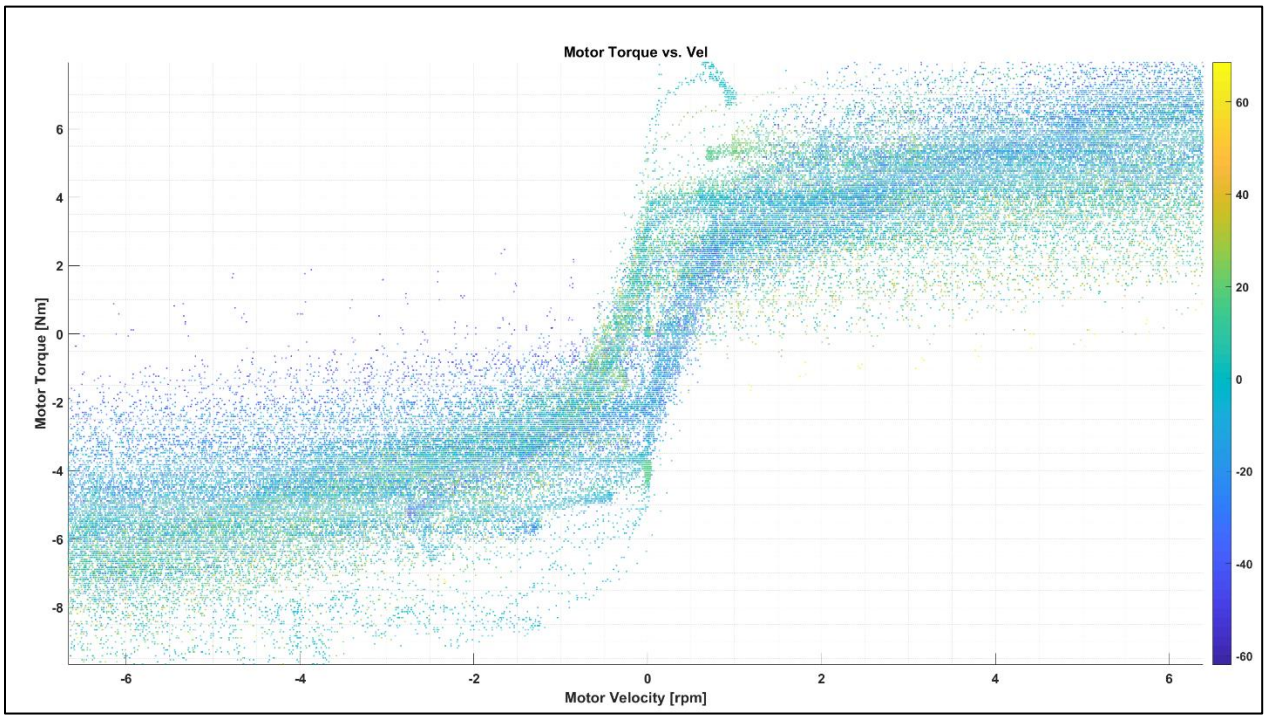

Figure 32: Details of the stiction characteristics of the combined motor-gearbox couple. Only a very small torque of roughly 4 Nm is required to overcome the combined stiction.

5.3 ENTIRE DRIVESHAFT

In order to get an estimate for the stiction as well as the viscous friction of the entire PTO shaft including all bearings and seals, various torque white noise signals were used as a torque setpoint command for the motor. As only the viscous friction of the shaft acts as a counter force against the motor torque once the stiction is overcome, these experiments are limited by the motor maximum velocity and thus the peak excitation torque for the noise excitation.

Multiple experiments with excitation magnitudes of 15Nm, 25Nm, 35Nm, as well as 40Nm were conducted with a total of 3 different phase white noise realizations and 3 repeats of 500 seconds each. Data obtained from these experiments are then used to plot the characteristic stiction/friction curve for the entire PTO shaft. Figure 33, Figure 34, Figure 35, as well as Figure 36 show the characteristic curves for the above mentioned peak excitation torques.

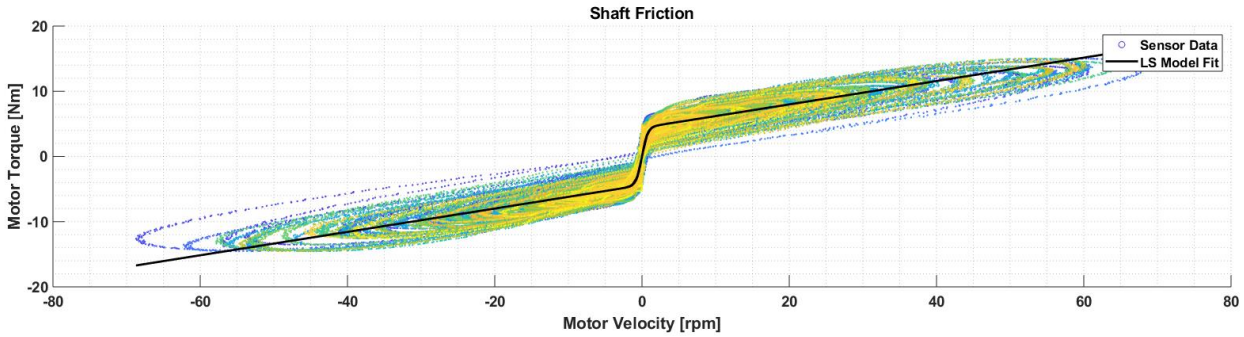

Figure 33: Characteristic stiction/friction plot for the entire PTO shaft. A Least Squares grey box model with hyperbolic tangents characteristic is used to model the stiction. (15 Nm peak)

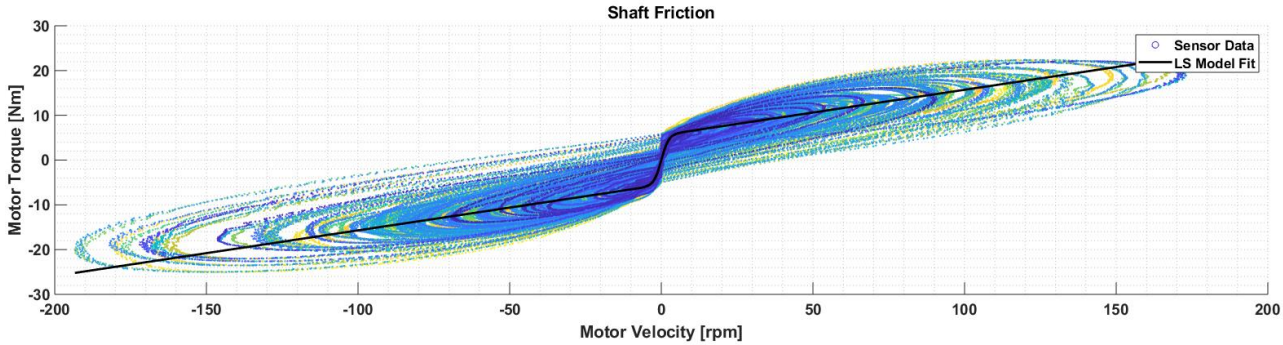

Figure 34: Characteristic stiction/friction plot for the entire PTO shaft. A Least Squares grey box model with hyperbolic tangents characteristic is used to model the stiction. (25 Nm peak)

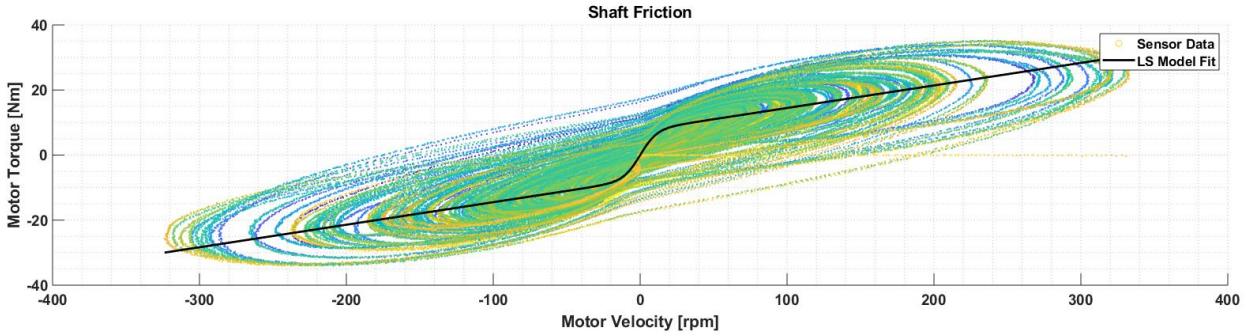

Figure 35: Characteristic stiction/friction plot for the entire PTO shaft. A Least Squares grey box model with hyperbolic tangens characteristic is used to model the stiction. (35Nm peak)

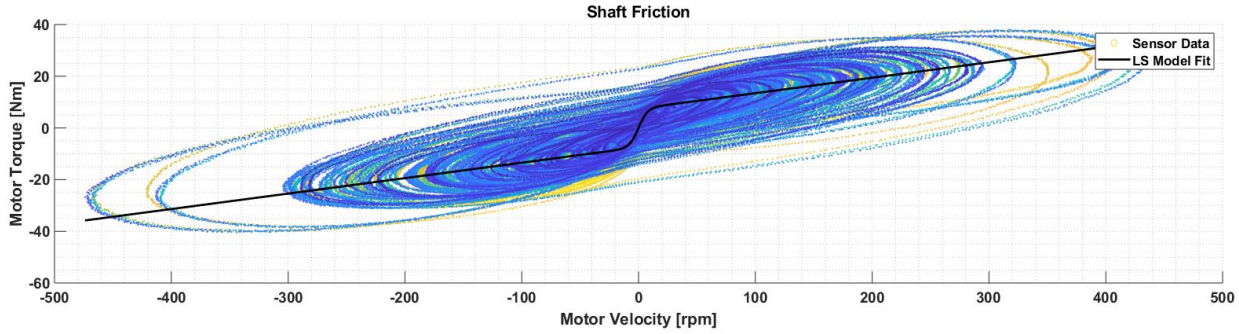

Figure 36: Characteristic stiction/friction plot for the entire PTO shaft. A Least Squares grey box model with hyperbolic tangents characteristic is used to model the stiction. (40 Nm peak)

Friction characteristics of the entire driveshaft appear very symmetric around the zero-velocity point, indicating that stiction and friction is symmetric in both directions.

In general, the total stiction of the dead band can be overcome by a motor torque of approximately 10-15 Nm, which is about 2.5 % - 3.75% of the continuous rated motor torque or 1.25% - 1.87% of the peak instantaneous torque capability of the motor. Note, that this dead band torque is on the motor side of the gearbox. Accounting for the gear ratio of 9:1, the dead band stiction on the shaft is about 90Nm – 135Nm.

Using an average mooring drum belt radius of 0.18m, the above indicated dead band leads to a linear force on the PTO belt of ~480 N which is about 4% of the static pre-tension on the belt for a common operating case. Furthermore, it is obvious that the stiction of the driveshaft becomes less important for the global characteristics as the rotating inertia of the shaft carries the mass through the stiction dead band for cases with higher velocity, respectively excitation motor torque. This is clearly visible in the more continuous, spread out friction characteristic when comparing the 40 Nm peak friction plot with the 15 Nm peak plot.

To model the characteristics dynamics including friction and stiction of the entire driveshaft a least square grey box model fit is used. As a friction model the common summation for Stribeck friction, and velocity dependent/viscous friction is utilized:

$$F = a * \tanh\left(\frac{dx/dt}{b}\right) + c * dx/dt$$

Due to the large amount of data collected in relatively short time, accurate model fits can be obtained. The models are plotted in addition to the collected data in the above figures.

The model fits for the above excitation magnitudes are presented in Table 3.

Table 3: Friction and Stiction Model Parameter for the entire PTO drive shaft.

Friction and Stiction Model parameter for the entire PTO drive shaft				
Peak Torque	15	25	35	40
a	4.402	5.531	7.555	7.468
b	0.7455	2.355	11.39	7.59
c	0.1792	0.1017	0.06926	0.05977

6. PTO Belt Testing

6.1 PTO Belt Design Basis

The PTO reacts against the sea floor for energy capture and controlling the linear force and displacement in the mooring lines that anchor the device is a primary control challenge. While conceptually simpler, a linear PTO would necessarily have limited stroke, introducing a risk of end-stop impacts and complicating installation and depth change operations. A primarily rotary PTO was chosen to avoid these limitations, but a linear-rotary conversion step is needed to interface the PTO and mooring lines.

We began the investigation into winching lines with widely available synthetic mooring lines commonly used in the maritime industry, for example those made with Vectran or Dyneema. In general, these lines are stocked in many fiber configurations and a range of strength ratings well above our nominal linear tension. However, ropes with a circular cross-section are fundamentally vulnerable to degradation over many bending-straightening cycles in which the shear friction of individual fibers accumulates heat; this phenomenon is known as “cyclic bend over sheave”, or CBOS and is well known in the rope and winch industries. CBOS risk is inversely proportional to the ratio of sheave diameter and rope diameter (the “D/d ratio”), and so can be reduced by increasing pulley diameter or reducing rope diameter. Still, rope manufacturers have only extended CBOS life to around 150,000 cycles; we expect >3 million bending cycles in our demonstration deployment, and so stock ropes will not work for our linear-rotary conversion step.

Given that the core problem is heat entrapment inside the rope itself, one solution is to increase the ropes surface area, leading to wide, flat belt shape instead of a conventual rope. A belt of nominally sufficient tensile strength was purchased from TTS Innova, shown in Figure 37.

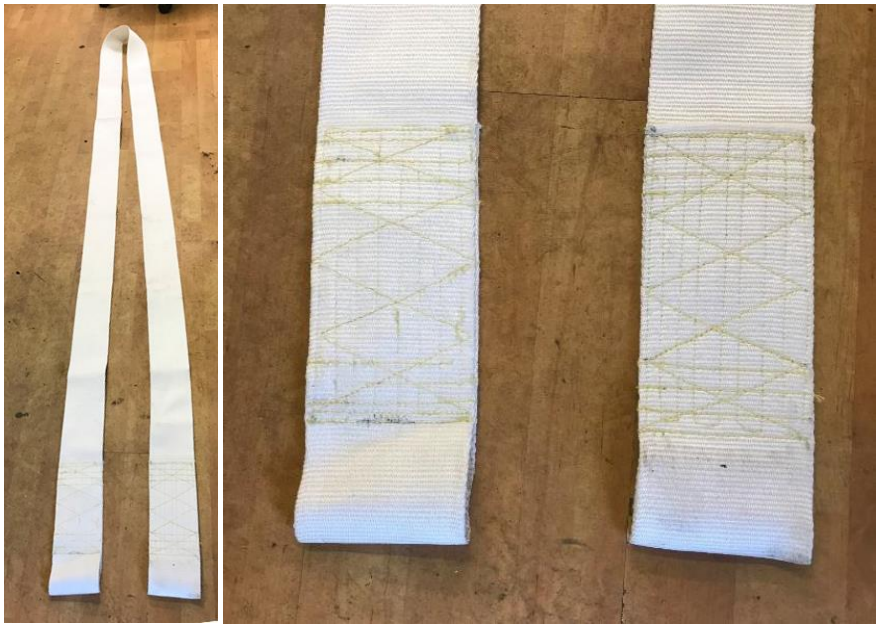

Figure 37: TTS Innova synthetic flat belt sample.

6.2 PTO Belt Testing

Testing of the TTS Innova woven synthetic fiber belts was conducted independently by two partners with special experience and equipment.

6.2.1 CBOS Testing at IFREMER

IFREMER conducted CBOS testing at their facility in France; the test procedures and results are found in the accompanying "CBOS Test on CPT HMPE Belt Test Report". The belt failed prior to enduring 100k cycles and fell short of the targeted millions of cycles. However, although the intent of the experiment was to test the CBOS performance of the HMPE belt, the actual failure mechanism appeared to be caused by abrasion along the belt edges due to the belt not fitting properly inside the sheave. A properly sized belt and sheave pair is expected to significantly increase the belt life. The delamination of the belt noted in Figure 2.17 also brings to question whether a fully woven cross section would be more robust than the layered one. It is also expected that upgrading to a branded fiber, such as DSM's Dyneema or Honeywell's Spectra, could increase fiber performance. Fiber manufacturers also have developed special coatings such as DSM's XBO coating which claim improved CBOS performance. Additional testing on an improved belt and sheave that incorporates the learnings is considered before the technology can be implemented in the scaled deployment reliably.

As a secondary result, load levels and temperatures caused by this testing induced very little creep elongation of the fibers. It is possible that with a shorter oscillation, the belt would reach higher temperatures than found in this experiment. Nevertheless, the low temperatures recorded are thought to leave sufficient margin before heating of the fibers becomes a real concern.

6.2.2 Shock Load Testing at Exeter

The University of Exeter, in England, conducted linear shock-load testing their Dynamic Marine Component (DMaC) testing facility; test setup and results are found in the accompanying "Taut Mooring Shock Load Testing" report. DMaC concluded that the woven HDPE belt concept can be a strong component, capable of tensile loads over 200kN. The "weak link" in a HPDE belt is the post-construction stitching, in this case of loop terminations. When a pin or shackle is fit through the loop, forces not aligned with the tension (i.e., not along the belt's strongest vector) can rip at the stitching and cause the belt to fail. This can be mitigated by increasing the loop length, thus decreasing the angle subtended by the two loop sides when wrapped around a pin or shackle.

APPENDIX A – EXAMPLE GAS SPRING SID RESULTS

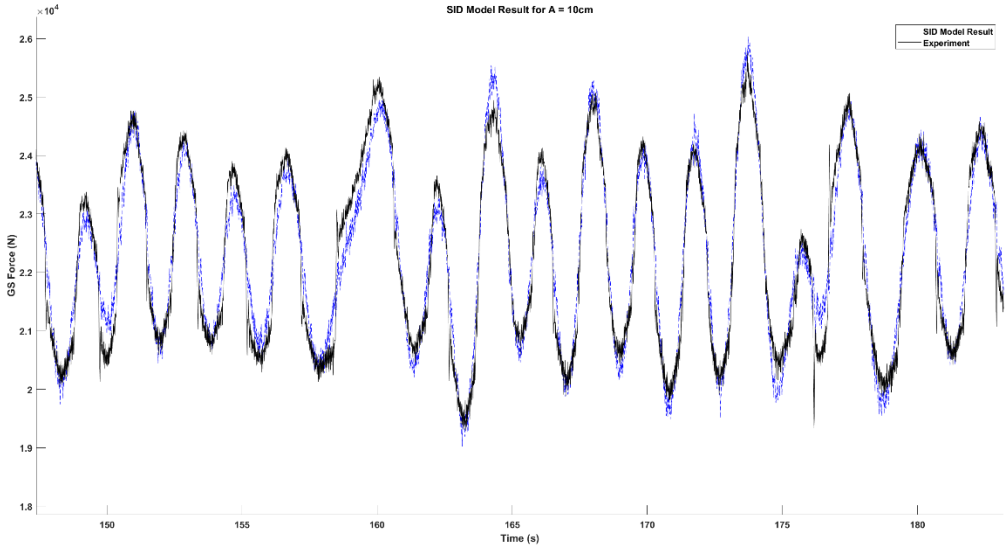

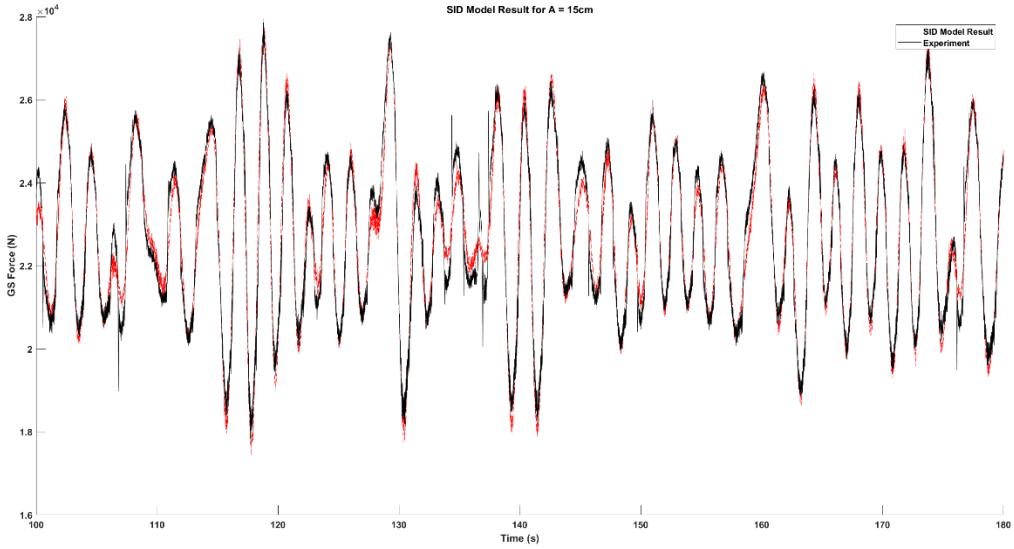

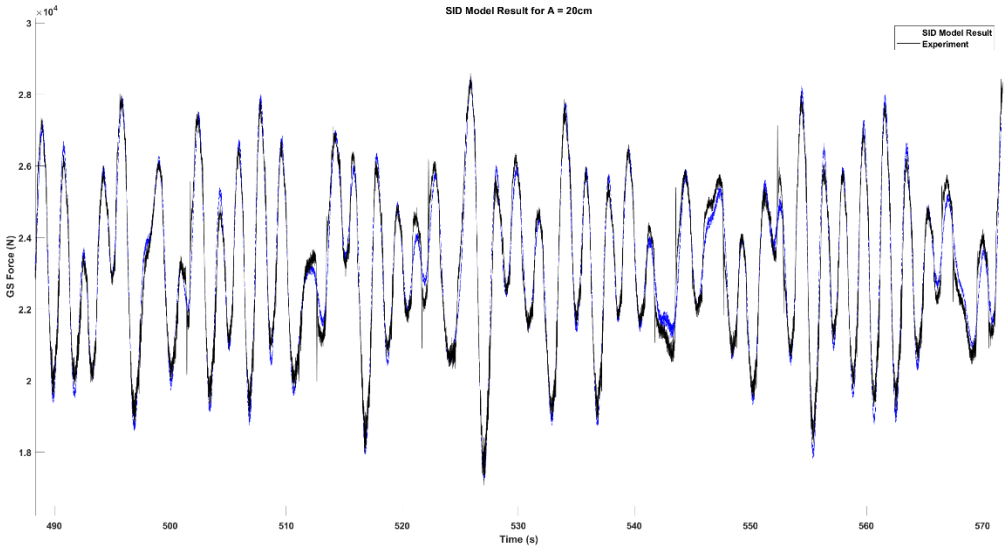
SID Model Result for A = 20cm
SID Model Result
Experiment
GS Force (N)
Time (s)

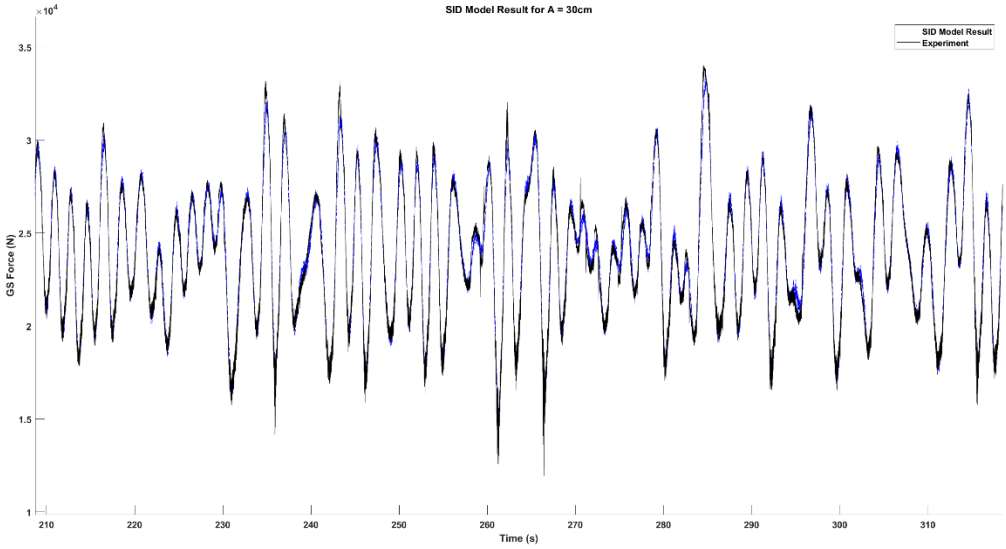
SID Model Result for A = 30cm
SID Model Result
Experiment
GS Force (N)
Time (s)

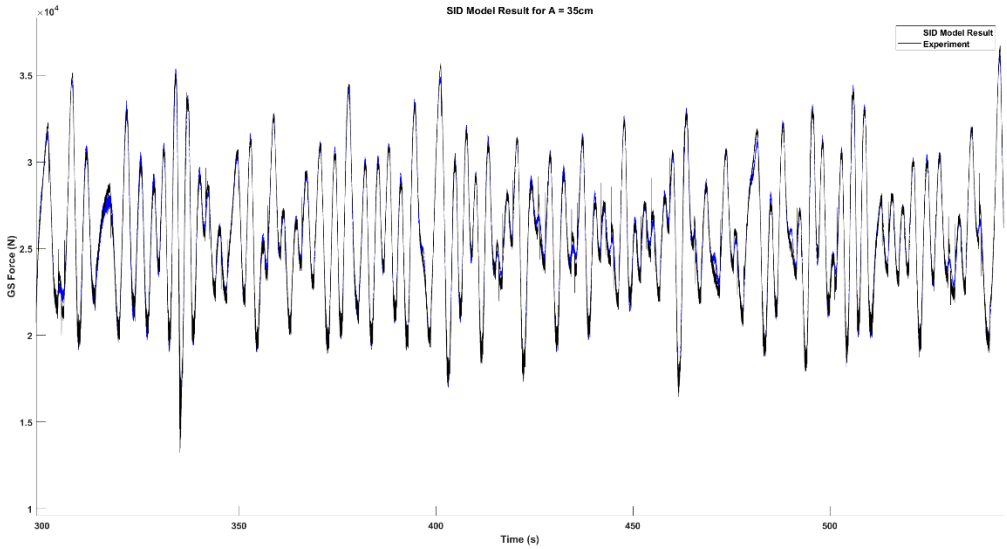
SID Model Result for A = 35cm
SID Model Result
Experiment
×10^4
3.5
3
2.5
2
1.5
1
GS Force (N)
300
350
400
450
500
Time (s)